CHAPTER 6

APPLICATION TO REAL CASES

The ultimate use of numerical models, that is, their application to real cases, is illustrated in this chapter. The selected cases correspond to different locations along the Catalan coast, and involve the use of both hydrodynamic and dispersion models, as well as data measured during several field campaigns and remote-sensing images.

All the cases presented here have been selected with the aim of testing different features of the transport model in various scenarios and under different environmental conditions.

The first study is purely qualitative, since no experimental data were available for comparison, and involves the dispersion of sewage from the Besòs marine outfall, just north of Barcelona. The wastewater discharge from this set of diffusers is modelled for different water stratification conditions, and the results are compared between them. This case was intended to check the performance of the buoyancy module implemented in the model and the algorithm proposed by Massel (1989) to obtain wind-induced current profiles from a 2DH velocity field.

A similar qualitative approach is followed in the last test case, corresponding to the settling of sediment transported by the Francolí river, and discharged into the Tarragona harbour. In this case the sediment settling module was tested, and a simple and straightforward way of including sediment resuspension was tried, as an alternative to more elaborate formulations.

The two remaining cases compare computational results with observational data or images, and are both located at the region of the Ebre delta. The first one deals with the dispersion of a cloud of tracer released in the surf zone at the Trabucador Bar. The results are compared to parameters obtained from digitised video recordings, which are used basically to verify the random walk module in a real case, and to derive the time-dependence of the dispersion coefficients.

The second remaining case is intended to calibrate the dispersion coefficients for the river Ebre's freshwater plume under different meteorological and river flow conditions. In particular, the behaviour of the river plume for summer and winter conditions is modelled, and the results are compared to data measured during two corresponding field campaigns (PIONEER II and PIONEER IV, respectively). An additional, albeit qualitative, comparison is done between the river plume modelled for summer conditions and the plume observed in a remote-sensing image.

6.1 THE BESÒS MARINE OUTFALL (BARCELONA, SPAIN)

The Besòs water treatment plant has the capacity to process nearly 500,000 m^3 of sewage water per day. Almost 60% of this volume is urban wastewater from the inhabitants of the Metropolitan Area of Barcelona (approx. 3.5 million inhabitants), whereas the rest is of industrial origin. The plant performs a physical and chemical treatment of the received wastewater before it is discharged, by means of a marine outfall, at a distance of 2,900m from the shore (figure 6.1), and at 50m depth. The diffuser length at the end of the outfall includes 15 risers, with a 50m separation between them, each one with four horizontal nozzles. The mean discharged flux is approximately 9.2 m^3/s.

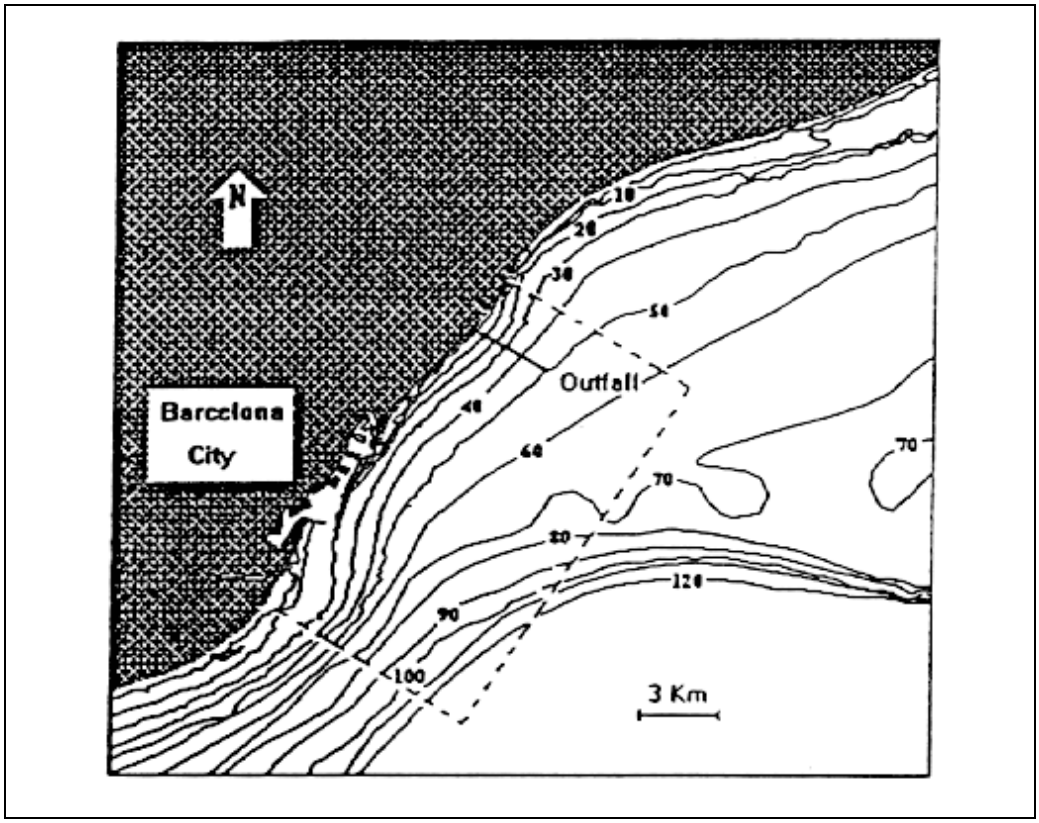

Figure 6.1: Location of the Besòs marine outfall, near Barcelona (Spain); the broken line defines the computational domain.

A simple qualitative test case involving the sewage discharge from the Besòs outfall was simulated using the hydrodynamic model NEARCIR (Sánchez-Arcilla *et al.*, 1992) and the LIMMIX dispersion model, in order to assess the performance of the dispersion model in its early development stages.

6.1.1 The hydrodynamic model NEARCIR

The numerical code NEARCIR (Sánchez-Arcilla *et al.*, 1990) is a depth-averaged two-dimensional hydrodynamic model that describes currents, waves, and wave-current interaction in coastal waters. In the case of the currents module, which is the only one used here since it is assumed that the effects of the wave field on the plume dynamics can be neglected, the model uses an explicit finite difference scheme to solve a 2D version of the continuity and momentum equations, obtained after performing a spatial average over the water column, up to the free surface:

$$\frac{\partial M_i}{\partial x_i} = 0 \tag{6.1}$$

$$\rho h\left(\frac{\partial\left\langle\overline{U_i}^{\eta}\right\rangle}{\partial t}+\left\langle\overline{U_j}^{\eta}\right\rangle\frac{\partial\left\langle\overline{U_i}^{\eta}\right\rangle}{\partial x_j}\right)+\frac{\partial\tilde{S}_{ij}}{\partial x_j}=-\rho g h\frac{\partial\langle\eta\rangle}{\partial x_i}+\frac{\partial\left\langle(\eta-z_0)\overline{s_{ij}^{T}}^{\eta}\right\rangle}{\partial x_i}+\langle\Delta\tau\rangle_i^{\eta} \tag{6.2}$$

where M is the water mass, $<\overline{U_i}^{\eta}>$ is a velocity associated to the mean mass flow over the water column, η is the free-surface level, z_0 is a reference level -usually the sea bed level-, h is the water depth, ρ is the water density, $\tilde{S}_{ij}$ is the radiation stress tensor, s_{ij}^{T} corresponds to the turbulent stresses at a given depth z, and $\langle\Delta\tau\rangle$ is the difference between the stresses at the top and at the bottom of the water column. In these equations, the Einstein summation convention has been adopted.

The turbulent correlations and other stresses appearing in equation (6.2) are solved using different closure models. In the first case, the correlations are estimated as

$$\left\langle(\eta-z_o)\overline{s_{ij}^{T}}^{\eta}\right\rangle=\frac{1}{2}\nu_{ij}h\left(\frac{\partial}{\partial x_j}\left\langle\overline{U_i}^{\eta}\right\rangle+\frac{\partial}{\partial x_i}\left\langle\overline{U_j}^{\eta}\right\rangle\right) \tag{6.3}$$

whereas the top and the bottom stresses are assumed to follow the general square velocity law,

$$\langle\boldsymbol{\tau}_b\rangle=\rho C_b\langle\mathbf{U}\,|\mathbf{U}|\rangle \tag{6.4}$$

$$\langle\boldsymbol{\tau}_w\rangle=\rho C_w\langle\mathbf{U}_w|\mathbf{U}_w|\rangle \tag{6.5}$$

where C_b and C_w are drag coefficients, $\boldsymbol{\tau_b}$ and $\boldsymbol{\tau_b}$ are the bottom and wind-induced stresses, and $\boldsymbol{U}$ and $\boldsymbol{U_w}$ are the current and wind velocity 10 meters above the surface, respectively. The coefficient ν_{ij} appearing in equation (6.3) is obtained using different expressions found in the literature (De Vriend and Stive, 1987; Longuet-Higgins, 1970; or Battjes, 1983).

6.1.2 The modelled case

The NEARCIR hydrodynamic model was used to obtain the depth-integrated circulation pattern in the region, induced by a 10 m/s wind blowing from the NE. The computational domain stretched 22 km in the longshore direction, and 16.5 km in the cross-shore direction, divided in 300m-by-450m grid cells. The simulation was run for almost 7 hours (25,000 sec) in order to reach a stationary state. The resulting 2DH velocity field is shown in figure 6.2. It can be seen that the currents are almost parallel to the coast, in a general southwest direction, except nearest the shoreline; the maximum value of the velocity is approximately 0.2 m/s.

The three-dimensionality of the current field was reproduced by modifying the uniform 2DH velocity profiles using Massel's (1989) formulation (equations 2.25). The particular wind-induced profiles obtained at the centre of the nozzle configuration is shown in figure 6.3. Neither the NEARCIR model nor Massel's profiling formulation take into account the possible stratification of the water watercolumn. This is specially a drawback in the modelling of the currents in summer and autumn, when the water density gradient is of the order $5 \cdot 10^{-6}$ (Salat *et al.*, 1978).

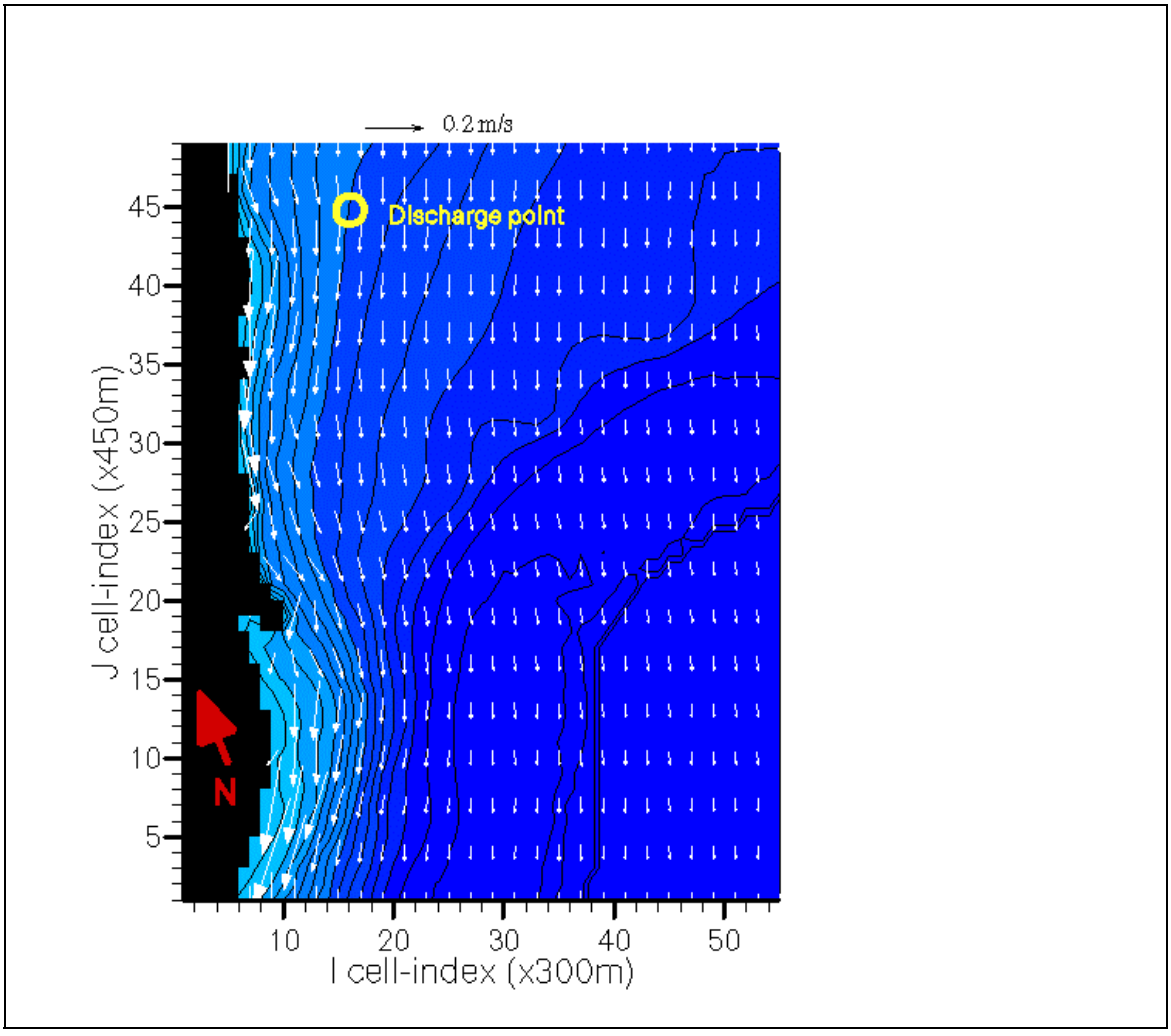

Figure 6.2: Current field induced by a 10 m/s wind, from the NE, in the Barcelona area. The solid circle shows the approximate outfall position.

For the dispersion simulation, two different environmental conditions have been considered; a first case assumes a water column stratification typical of the summer season, whereas the second represents a well-mixed waterbody (uniform density) characteristic of winter (figure 6.4). For both cases the discharge parameters are the same: Q = 9.1 m^3/s, $C_0 = 10^6$ bact/ cm^3, and T_{90} = 24 hours.

The results for the first case (summer stratification) are shown in figure 6.5, for the 10 risers located farther from the coastline. The corresponding plume has been calculated using a total of over 36,000 particles, released during a 30-min period, with a 3-sec computational timestep, and an effluent density equal to 1.026 g/cm^3. On the other hand, figure 6.6 presents the plume resulting from the outfall discharge under winter density conditions (i.e., unstratified water column), using 40,500 particles with a 4-sec timestep. In the former case, although the outer regions of the plume do reach the surface, the plume centreline and, thus, the maximum concentration regions, become trapped underwater because of the ambient density gradient. In the second case, the plume rise appears to be very fast because of the difference between the effluent density and the receiving water density (r_w = 1.0285 g/cm^3), although ambient water entrainment into the plume body should reduce density differences, decreasing the plume rise velocity and curbing its trajectory; the particles impinge the water surface and accumulate there, since the modelled vertical velocity is larger than the horizontal hydrodynamic velocities which should drag the particles away. These results were obtained using a formulation for the buoyancy term based on simple dynamic considerations, and illustrated the need to develop a more detailed buoyancy module, such as the one described in §5.2.1.3.

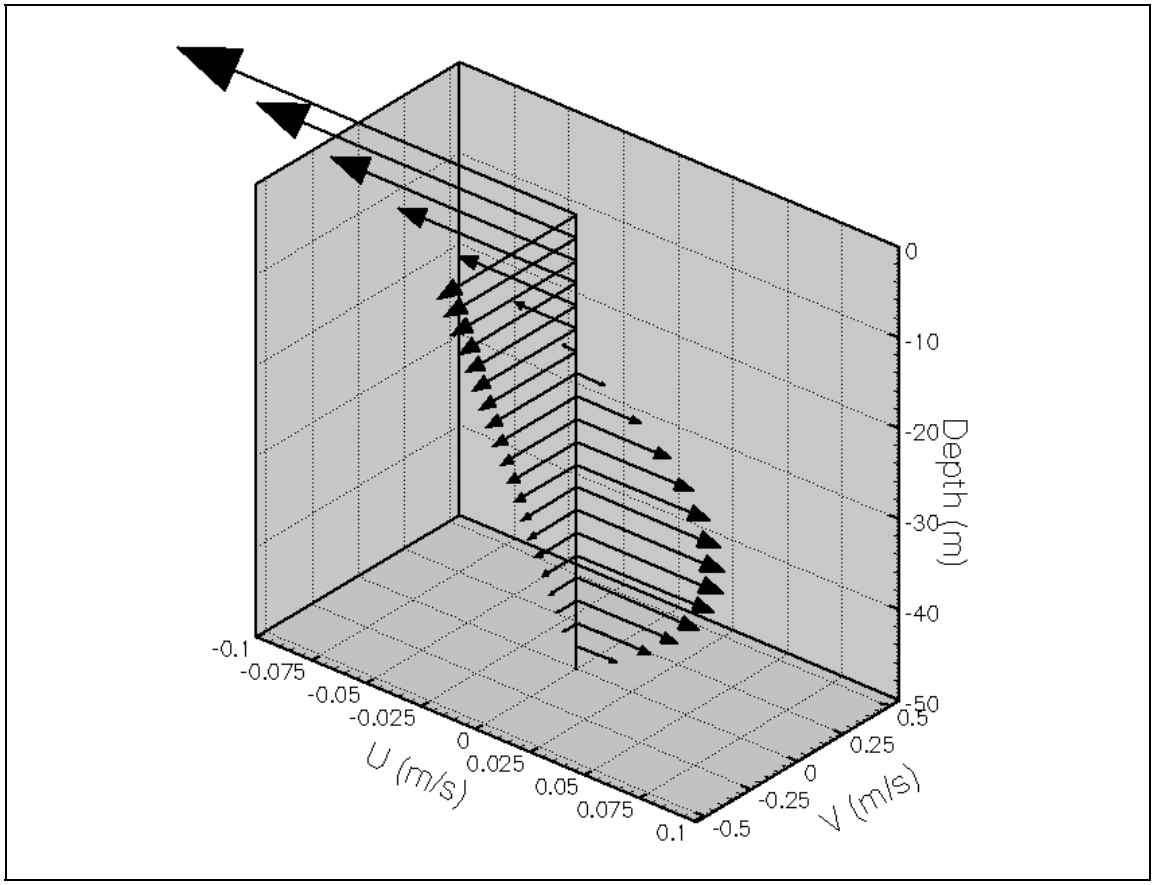

Figure 6.3: Wind-induced current profiles in the watercolumn just above the centre of the diffuser length, for the Besòs marine outfall.

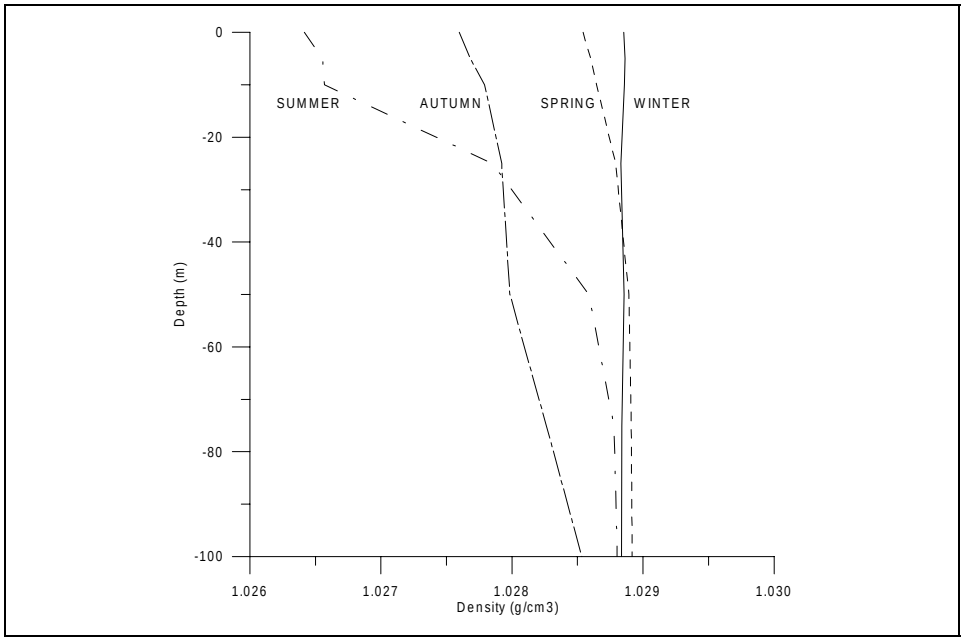

Figure 6.4: Typical density profiles off the coast of Barcelona (from measurements by Salat *et al.*,1978).

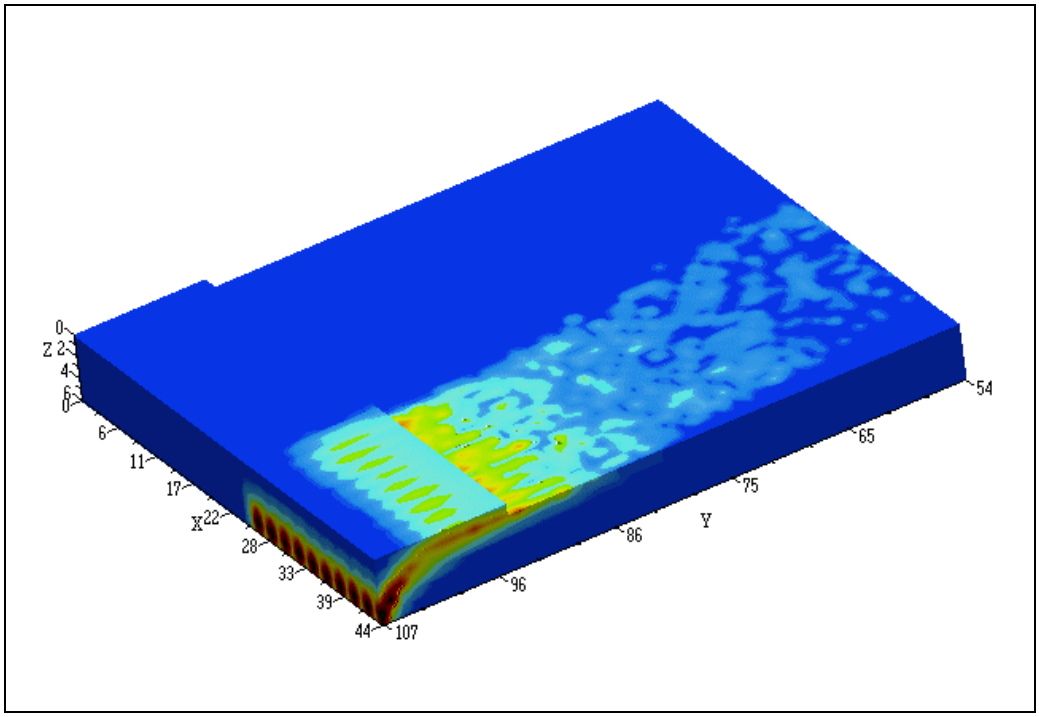

Figure 6.5: Effluent plume from the Besòs outfall under summer ambient density conditions.

Finally, a close-up of the discharge of an individual riser is shown in figure 6.7. It can be seen that the effluent from each one of the four horizontal nozzles merge into one single plume shortly after the discharge, immediately above the riser.

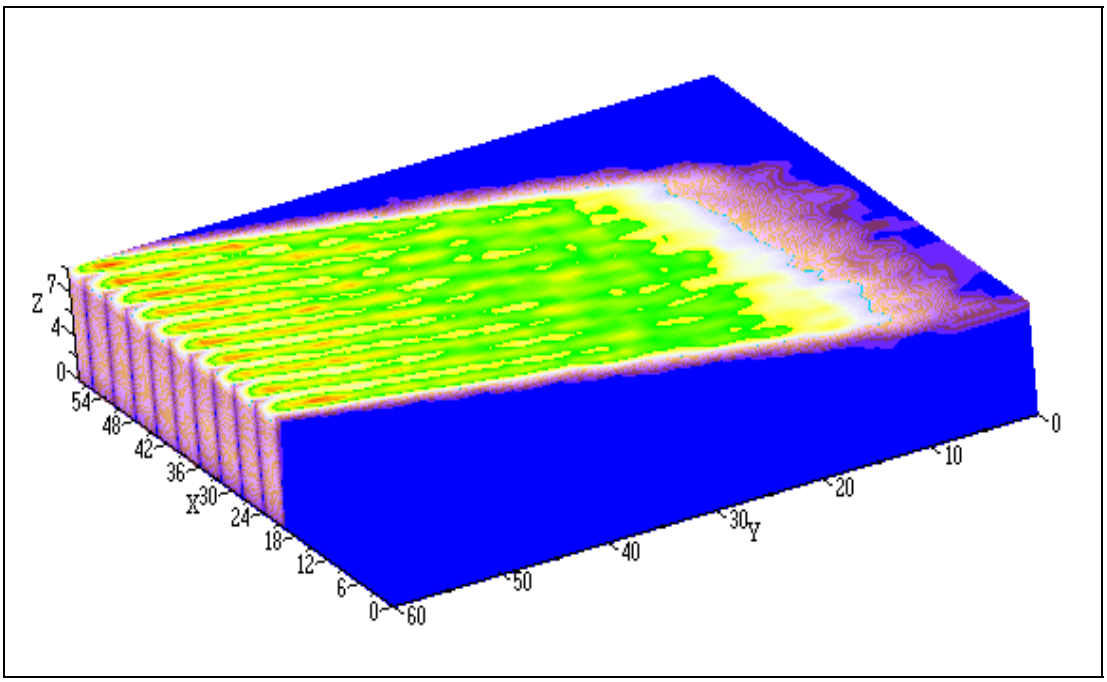

Figure 6.6: Effluent plume from the Besòs outfall under winter ambient density conditions.

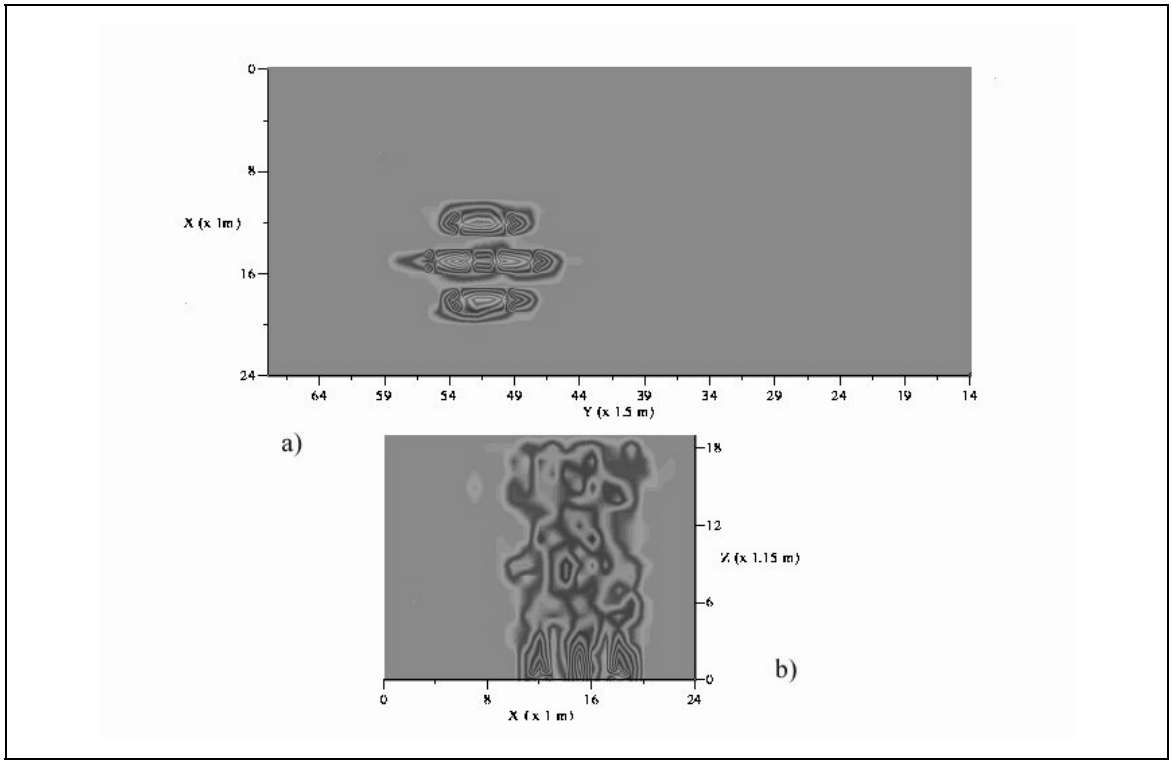

Figure 6.7: Close-up of the discharge from one of the risers, comprising four horizontal nozzles. **a)** Plan view; **b)** Vertical view.

6.2 A POINT SOURCE DISCHARGE AT THE TRABUCADOR BAR (EBRE DELTA, SPAIN)

During early November 1996, a set of large-scale hydromorphodynamic experiments was carried out at the Trabucador Bar, on the southern half of the Ebre delta (figure 6.8). This field campaign, named DELTA'96, was devised within the framework of the CIIRC international projects and the EU's FANS project (*Flow Across Narrow Shelves: The Ebre delta case*), and was participated by researchers from the Laboratori d'Enginyeria Marítima (LIM) at the Universitat Politècnica de Catalunya, and from other Spanish and Russian institutions; its main goal was to study, in an integrate manner, the meteorological and hydrodynamic processes, their interrelations, and their impact on the nearshore (Sánchez-Arcilla *et al.*, 1997).

One of the experiments carried out consisted in releasing tracer patches within the surf zone and videotaping their time evolution, in order to estimate the local turbulent mixing coefficients. For this purpose a set of two video cameras was used: one camera was assembled atop a 40m high crane, whereas the second was suspended from a 4m diameter helium-filled aerostatic balloon, moored above the experiment area. With this camera configuration, it was possible to acquire oblique and zenithal images of the tracer spots as they dispersed.

The images so obtained were later digitised using commercial software, and the time evolution of physical characteristics such as the patch size and concentration were then made available. An example of such digitised images, showing the tracer cloud at different times after its release is given in figure 6.9. A description of the digitalisation process, including the necessary coordinate transformations, can be found in Rodríguez *et al.* (1997). The experimental data were completed with simultaneous measurements of the current field near the tracer release point, using a sledge, which could be directed from the shoreline, equipped with a vertical array of currentmeters.

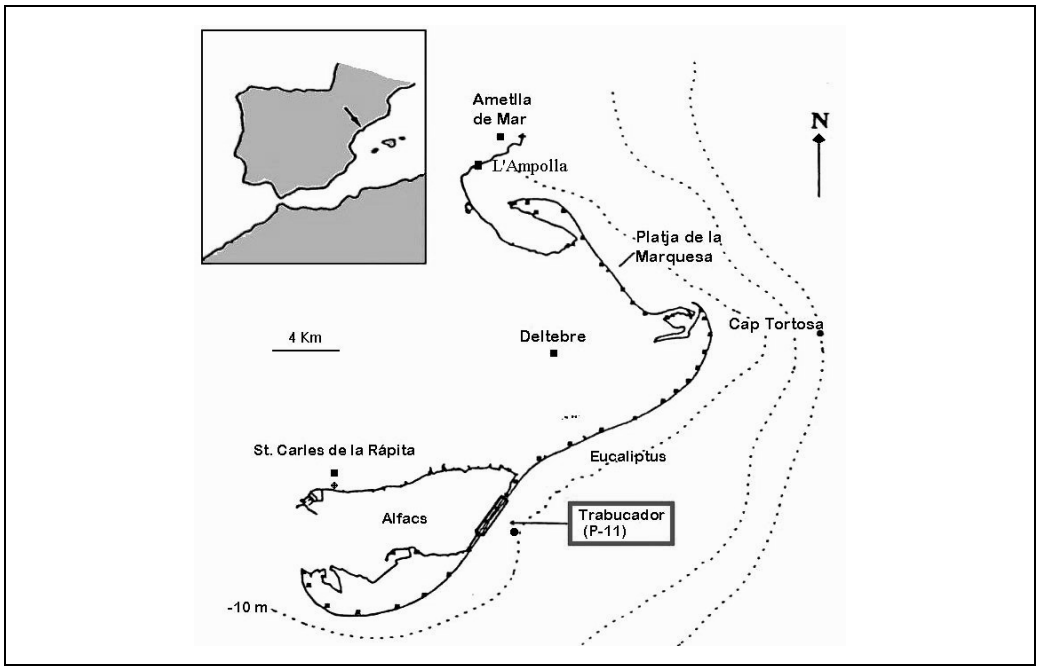

Figure 6.8: The Ebre delta and the Trabucador Bar, where DELTA'96 experiments were undertaken.

One of several measured tests was chosen to be modelled, and the corresponding images were selected. In order to reduce the effects of the wave field on the tracer patch images (see Rodriguez *et al.*, 1997), the wave period T_w was determined and images were chosen at timesteps equal to four times T_w. The maximum concentration of the cloud, and the patch diameters in the directions roughly parallel and normal to the cloud trajectory were extracted from these digitised images. In most of the images, the central region of the tracer cloud appeared saturated, and internal structure could therefore not be resolved. Because of this, the concentration distribution within the cloud was not modelled in this work, and effort was directed to the size of the cloud and its trajectory.

6.2.1 The hydrodynamic velocity field

The original goal was to use a hydrodynamic model to yield the current pattern in the area where recordings were done. However, velocity values during these experiments were obtained at one single point within the surf zone and, consequently, a validation of the modelled current field was difficult to achieve. To overcome this difficulty it was decided, after examining the sequence of images and observing that the path of the tracer cloud was roughly a straight line, to refer the tracer motion to a new set of axes *X*-*Y*, defined parallel and normal to the main direction of displacement, and to obtain a "longitudinal" and a "transverse" velocity component by comparing the tracer cloud position in two consecutive images, and dividing by the time interval between them. Figure 6.10 plots the position of the patch centres, taken from the series of images, referred to the longshore-cross-shore system, together with the new set of axes.

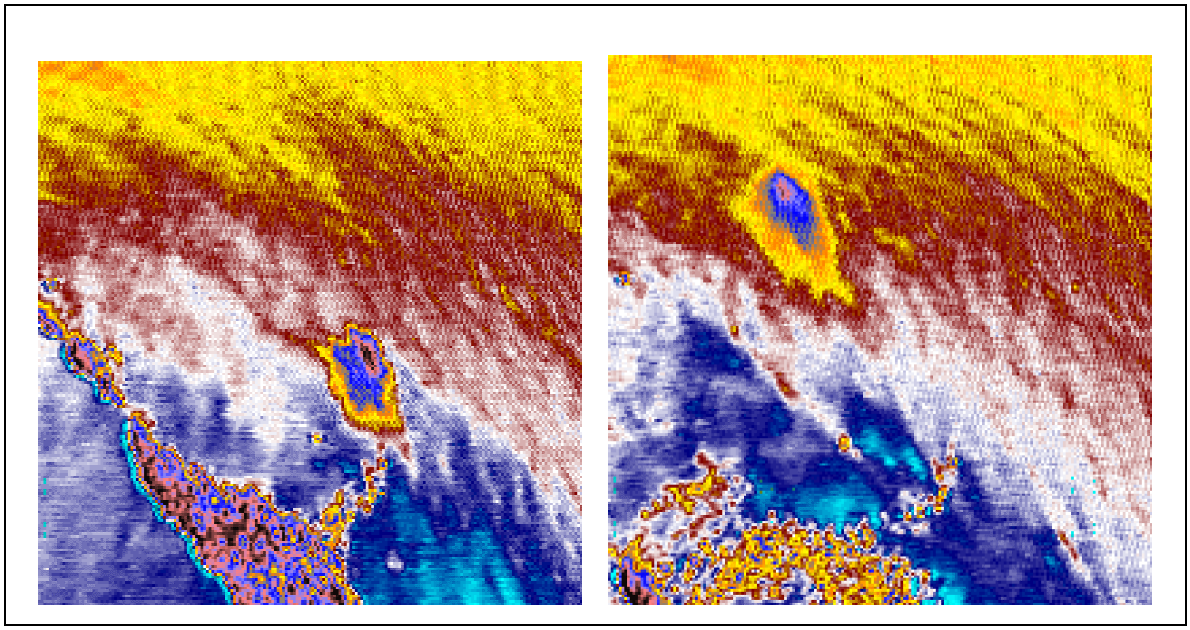

Figure 6.9: Video images of the tracer patch, after the digitalisation process. The images correspond to the patch 129 (left) and 417 (right) seconds after the tracer release.

6.2.2 Estimating the local mixing coefficients

In addition, local turbulent mixing coefficients were derived from the measured patch sizes in the new longitudinal and transverse directions, using the random walk equation for particle dispersion

$$\Delta r = \sqrt{6D\Delta t} \tag{6.6}$$

where Δr is the patch size, and D is the mixing coefficient in a given direction. The time evolution of the obtained values is shown in figure 6.11, together with best fits. The best fitting functions shown in this figure were used to furnish the different runs of the transport model.

6.2.3 Results

Four model runs, each one employing 5,000 particles, were done using the logarithmic and power expressions found above for the longitudinal and transverse diffusion coefficients. The patch sizes and the trajectory of the dye cloud centre referred to the system of reference *X-Y* were obtained, and are shown in figures 6.12, 6.13, 6.14, 6.15 and , respectively. Both the sizes and the position of the centre plotted in these figures are found by averaging the results of the four different model runs.

In figures 6.12 and 6.13, the tracer cloud dimensions yielded by using constant and time-varying diffusivities are compared to those obtained from image processing. It can be readily seen that the size of the patch in the longitudinal direction is reproduced with an acceptable degree of accuracy, whereas the results for the transverse dimension are not so good. These differences may be linked to a number of factors, including the effects of perspective due to the angle of the video recorder on the crane during image acquisition, or the effects of waves on the tracer image.

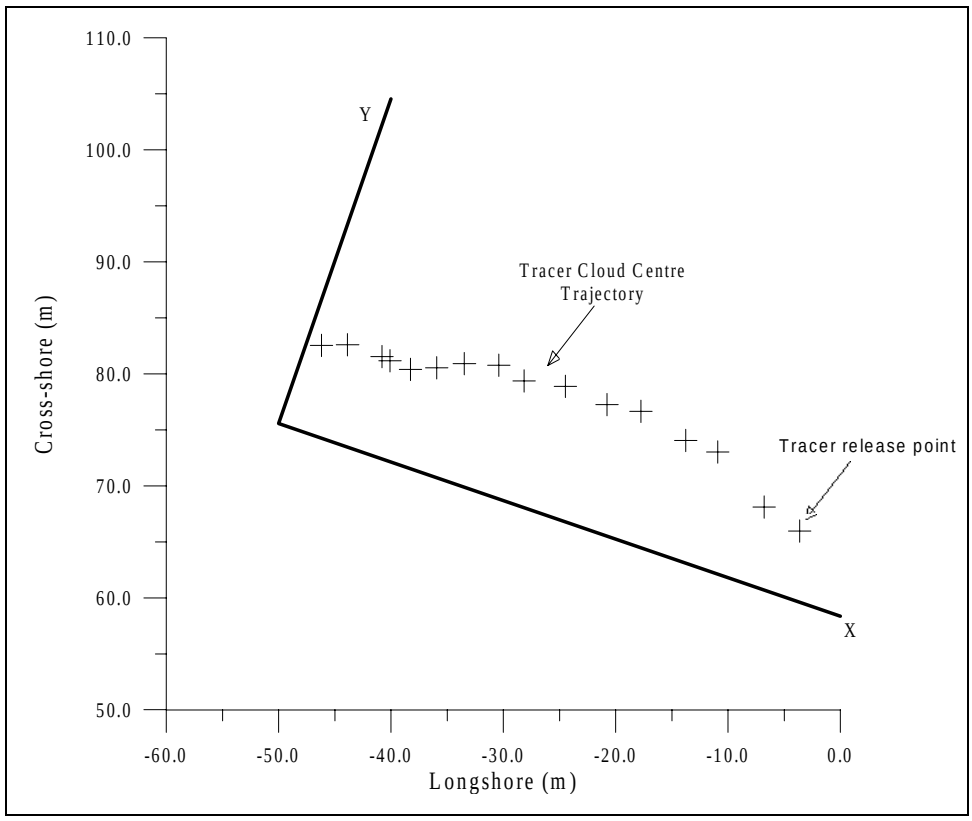

Figure 6.10: Tracer patch centre, referred to longshore-cross-shore reference system, and the new set of axes *X-Y*.

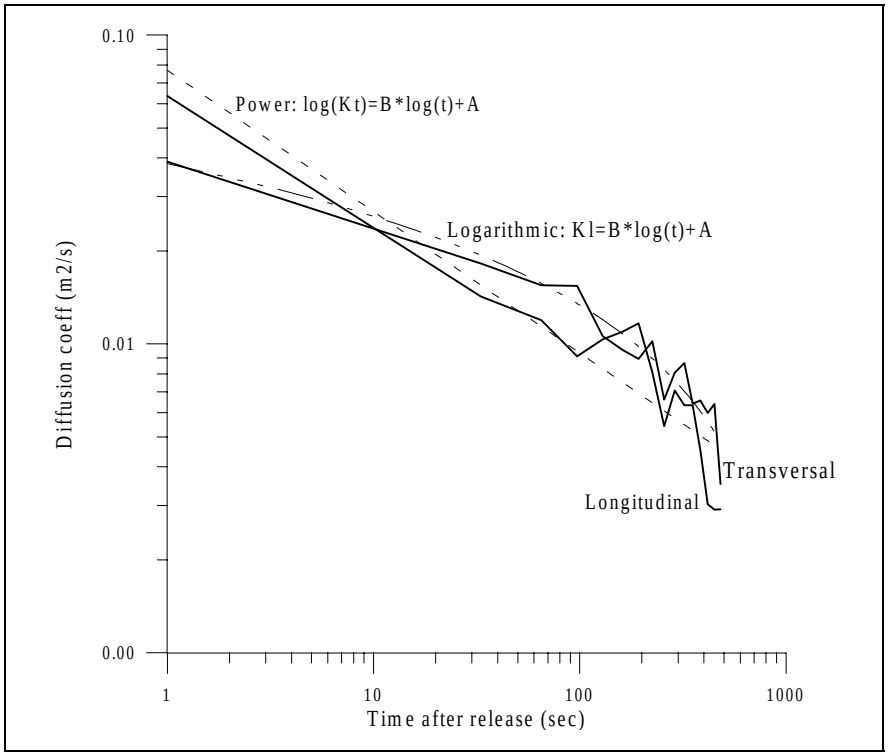

Figure 6.11: Longitudinal and transverse diffusion coefficients, from the video images. The solid lines are measured values; the broken lines are best fits.

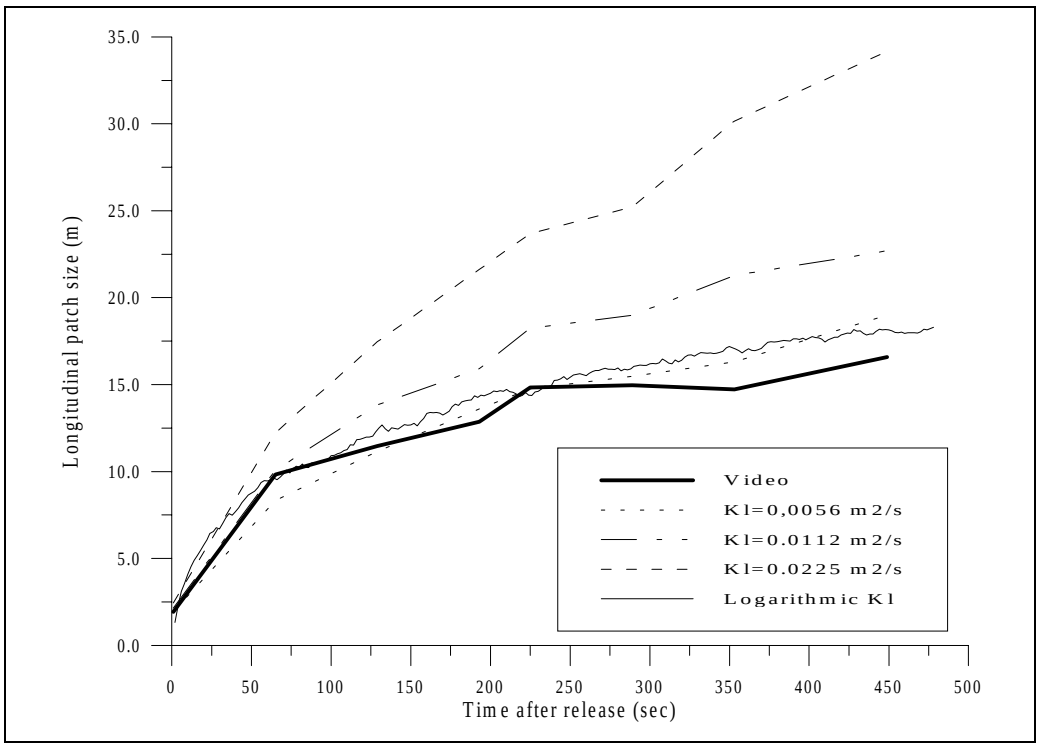

Figure 6.12: Tracer cloud size in the longitudinal direction, for different mixing coefficients, compared to that observed.

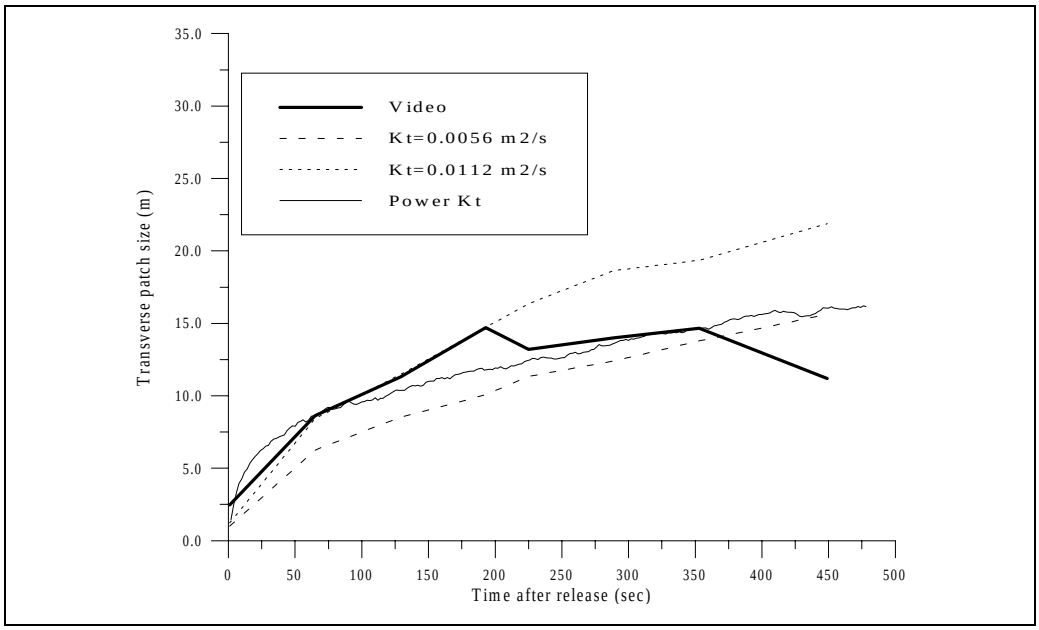

Figure 6.13: Tracer cloud size in the transverse direction, for different mixing coefficients, compared to that observed.

The simulation of the patch centre displacement is also satisfactory, even though it shows a similar problem to that of the patch dimension in the transverse direction. This is shown in figure 6.14, in which the observed and the modelled trajectories, referred to the auxiliary set of axes *X-Y*, are plotted. However, the overall behaviour of the modelled tracer cloud coincides with that observed in the video images, as is clearly reflected in figure 6.15.

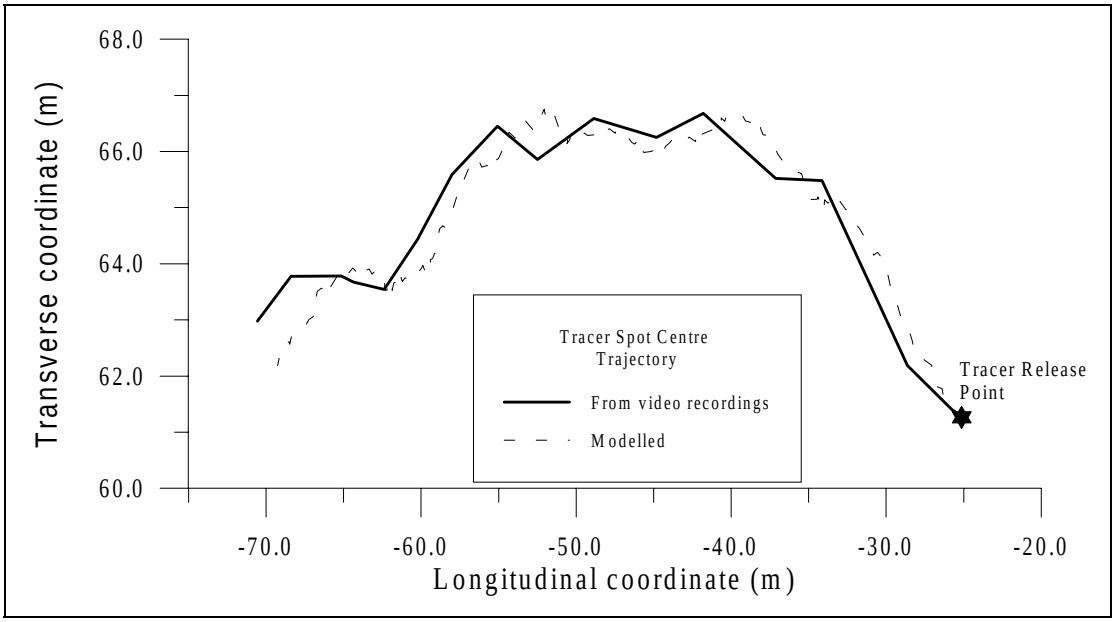

Figure 6.14: Tracer cloud trajectory, referred to the auxiliary set of axes *X-Y*.

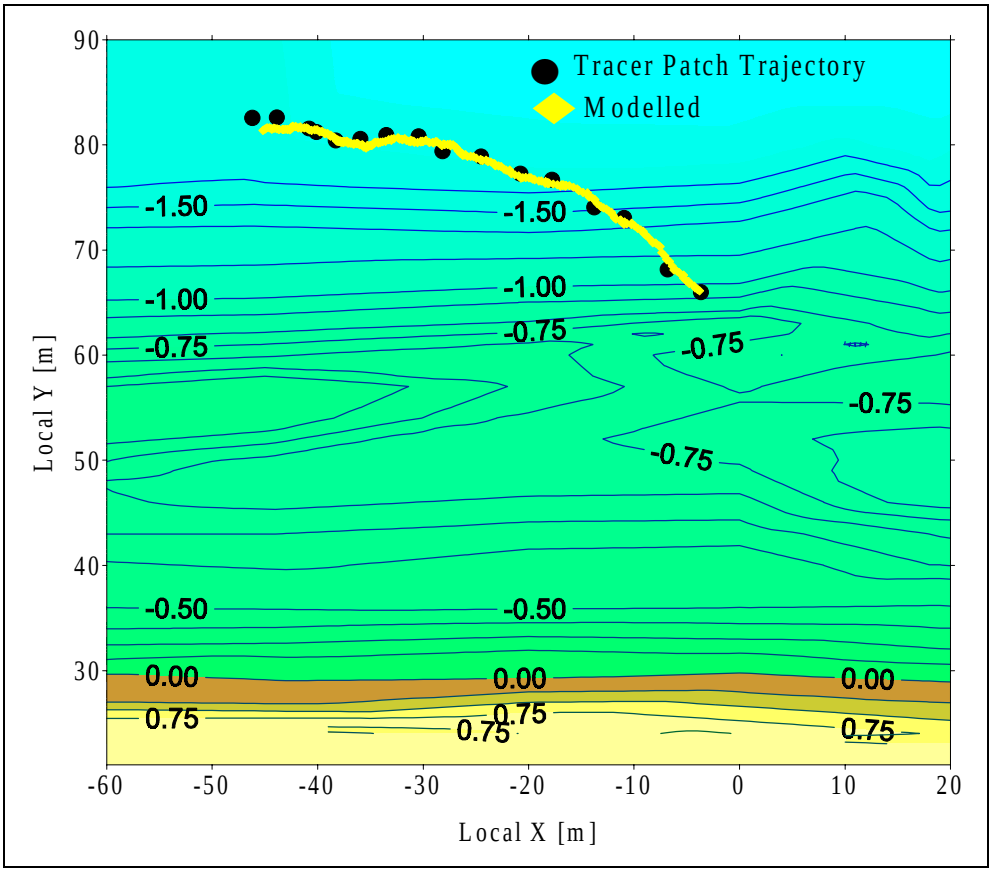

Figure 6.15: Tracer patch trajectory, in the longshore-cross-shore reference system.

6.3 THE RIVER EBRE PLUME

The estuary of the Ebre river, in the Western Mediterranean Sea (figure 6.8), is considered a micro-tidal environment in which the net river discharge into adjacent coastal waters depends strongly on the season of the year, and on local sea and weather conditions. The important role played by the sediments and nutrients transported by the river freshwater in relevant physical and biochemical processes in the sea extends beyond the Ebre delta region, as can be seen from the study of visible imagery obtained from satellites, which reveals that the river plume can be identified up to distances of several tens of kilometres offshore, even for small freshwater discharge rates.

Because the most important sectors of local economy, such as fisheries and tourism, are based on the sea, a good quality of the coastal waters at and near the Ebre river mouth becomes an essential parameter to be conserved. Therefore, it becomes desirable to have the ability and the tools necessary to allow the simulation of river plume behaviour, in order to monitor the evolution of the water quality in this area.

With this goal in mind, a hydrodynamic numerical model and the dispersion model LIMMIX have been combined, and the behaviour of the river plume has been modelled for different general conditions. Data obtained from the modelled plumes have then been quantitatively compared to measurements acquired during two field campaigns undertaken in the area in 1999 and 2000, and qualitatively with the river plume observed in a satellite image.

6.3.1 Brief description of the field campaigns

During 1999-2000, several field campaigns took place in the region of the Ebre delta, including the river, within the framework of the PIONEER project, funded by the European Union. These campaigns were aimed at studying the hydrodynamics of the coastal region, and the behaviour of the river plume under different (seasonal) wind, sea and river discharge conditions.

The two campaigns which are of concern here are those undertaken in July, 1999 and February, 2000 (i.e., summer and winter campaigns), named PIONEER II and PIONEER IV. The field work and laboratory post-processing of measurements and water samples involved the Laboratori d'Enginyeria Marítima (LIM/UPC), at the Universitat Politècnica de Catalunya, and the Laboratorio de Tecnologías del Medio Ambiente, at the Universitat Politècnica de Valencia. A complete description of these field campaigns can be found in Martínez *et al*. (1999, 2000), and only a brief description of their particular characteristics is given here:

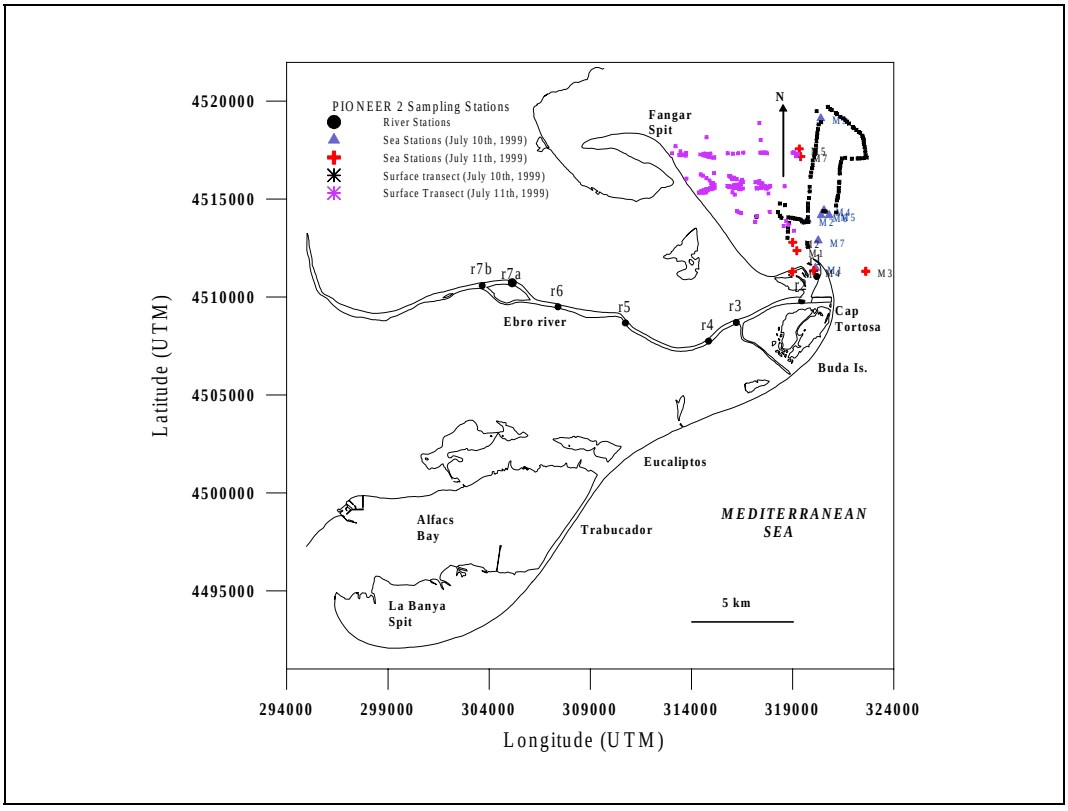

Figure 6.16: Position of the sampling stations and transects at the river and river plume (July 5th-13th, 1999).

6.3.1.1 PIONEER II (July 5th-13th, and July 16th-21st, 1999)

During this campaign, hydrodynamic and water quality measurements were done in three different domains, i.e., the river (approximately 19 km upstream from the river mouth), the estuary, and the river plume; the stations where measurements were done are shown in figure 6.16.

Hydrodynamic measurements consisted of detailed 2D and 3D current velocity profiles, together with values of the surface currents. CTD profiles were taken within the river domain, to

describe the salt wedge behaviour, and inside the river plume region, and pH, salinity, conductivity and temperature profiles were also obtained using a Hydrolab.

Water samples were taken at different depths in order to analyse nutrients (phosphorus, nitrates, nitrites, ammonium and silica), suspended matter, salinity, pH, phytoplankton, and chlorophyll. The data acquisition was completed with a thorough bathymetry scan of the river's last 40 km. In addition, meteorological data (wind speed and direction from the station at L'Ampolla –see figure 6.8) and river discharge data were supplied by external institutions.

6.3.1.2 PIONEER IV (February 1st-6th, 2000)

Measurements taken in this campaign include hydrodynamic data, water quality and biological parameters, and weather characteristics. The stations where measurements were obtained are shown in figure 6.17.

As in the previously described campaign, hydrodynamic measurements consisted of current velocity vertical profiles, and surface velocity data. CTD profiles and Hydrolab profiles were used to obtain data regarding water temperature, salinity, pressure, conductivity and pH, and again water samples were taken at different depths to provide information on nutrient concentrations, salinity, and phytoplankton content. As in the PIONEER II campaign, external institutions were responsible for supplying meteorological (from the station at L'Ampolla) and river discharge data.

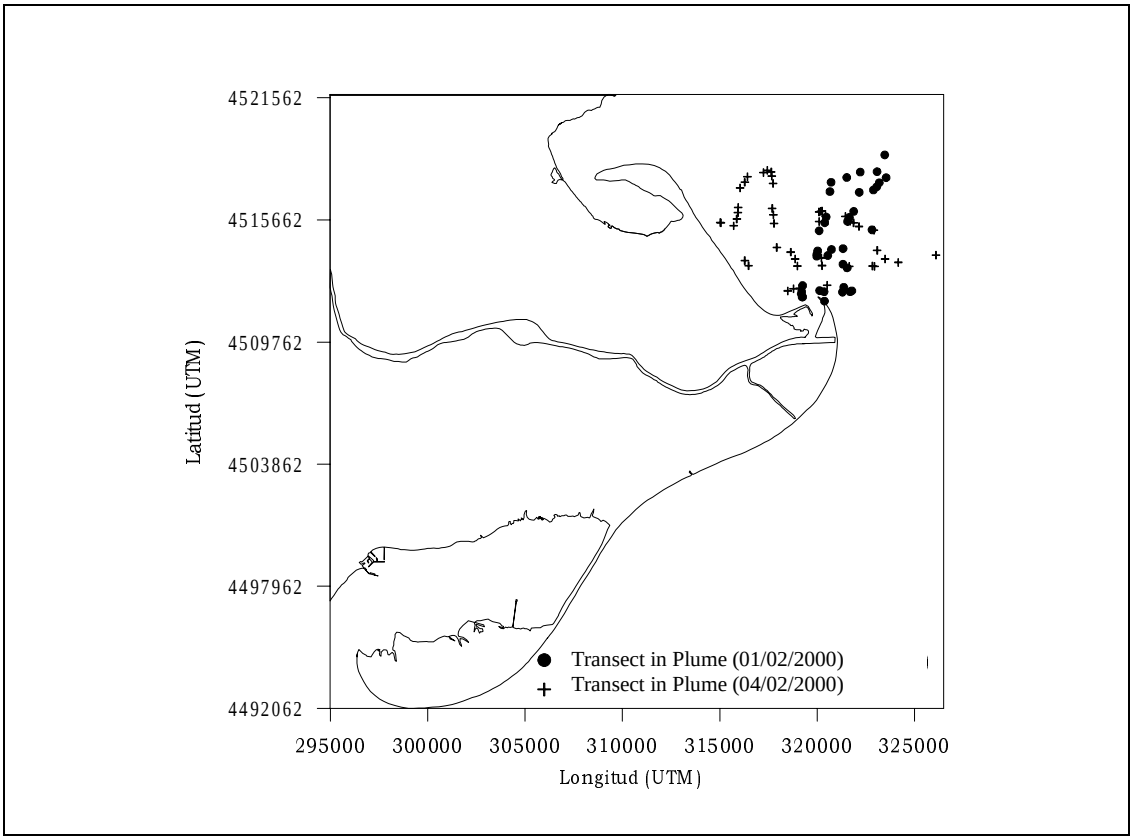

Figure 6.17: Position of the sampling stations and transects at the river and river plume (February 1st and 4th, 2000).

6.3.2 The hydrodynamic model TRIM3D

TRIM3D is a three-dimensional numerical model based on a semi-implicit finite difference approach to the governing primitive variable equations describing constant-density free surface flows, derived from the Navier-Stokes equations after turbulent averaging and under the assumption that pressure $p(x, y, z)$ can be expressed as the sum of a hydrostatic component $g[\eta(x, y, z)]$ and a hydrodynamic component $q(x, y, z)$ (Casulli and Stelling, 1996),

$$\frac{\partial u}{\partial t}+u\frac{\partial u}{\partial x}+v\frac{\partial u}{\partial y}+w\frac{\partial u}{\partial z}=-g\frac{\partial \eta}{\partial x}-\frac{\partial q}{\partial x}+\nu_H\left(\frac{\partial^2 u}{\partial x^2}+\frac{\partial^2 u}{\partial y^2}\right)+\frac{\partial}{\partial z}\left(\nu_V\frac{\partial u}{\partial z}\right)+fv \tag{6.7}$$

$$\frac{\partial v}{\partial t}+u\frac{\partial v}{\partial x}+v\frac{\partial v}{\partial y}+w\frac{\partial v}{\partial z}=-g\frac{\partial \eta}{\partial y}-\frac{\partial q}{\partial y}+\nu_H\left(\frac{\partial^2 v}{\partial x^2}+\frac{\partial^2 v}{\partial y^2}\right)+\frac{\partial}{\partial z}\left(\nu_V\frac{\partial v}{\partial z}\right)-fu \tag{6.8}$$

$$\frac{\partial w}{\partial t}+u\frac{\partial w}{\partial x}+v\frac{\partial w}{\partial y}+w\frac{\partial w}{\partial z}=-\frac{\partial q}{\partial z}+\nu_H\left(\frac{\partial^2 w}{\partial x^2}+\frac{\partial^2 w}{\partial y^2}\right)+\frac{\partial}{\partial z}\left(\nu_V\frac{\partial w}{\partial z}\right) \tag{6.9}$$

$$\frac{\partial u}{\partial x}+\frac{\partial v}{\partial y}+\frac{\partial w}{\partial z}=0 \tag{6.10}$$

where ν_H and ν_V are the horizontal and vertical turbulent viscosities, and f is the Coriolis parameter.

The model formulation also includes the following free-surface equation:

$$\frac{\partial \eta}{\partial t}+\frac{\partial}{\partial x}\left(\int_{-h}^{\eta} u\,dz\right)+\frac{\partial}{\partial y}\left(\int_{-h}^{\eta} v\,dz\right)=0 \tag{6.11}$$

and the boundary conditions at the free surface and at the sea bed are specified by the prescribed wind stresses and the bottom (friction) stresses, respectively.

The solution method is derived from a fractional step scheme. In the first step, the hydrodynamic component of the pressure is neglected, and the gradient of surface elevation on the horizontal momentum equations and the velocity in the free surface equation are discretised implicitly for the sake of stability. The resulting equations are rather cumbersome (Casulli and Stelling, 1996), and will not be given here.

In the second step, the hydrodynamic pressure is determined by requesting that the new velocity field is divergence free, which leads to a finite difference Poisson equation

$$\Delta t\left[\frac{\left(q^{n+1}_{i+1,j,k}-q^{n+1}_{i,j,k}\right)\Delta z^{n+1}_{i+1/2,j,k}-\left(q^{n+1}_{i,j,k}-q^{n+1}_{i-1,j,k}\right)\Delta z^{n+1}_{i-1/2,j,k}}{\Delta x^{2}}+\right.$$
$$+\frac{\left(q^{n+1}_{i,j+1,k}-q^{n+1}_{i,j,k}\right)\Delta z^{n+1}_{i,j+1/2,k}-\left(q^{n+1}_{i,j,k}-q^{n+1}_{i,j-1,k}\right)\Delta z^{n+1}_{i,j-1/2,k}}{\Delta y^{2}}+$$
$$\left.+\frac{\left(q^{n+1}_{i,j,k+1}-q^{n+1}_{i,j,k}\right)}{\Delta z^{n+1}_{i,j,k+1/2}}-\frac{\left(q^{n+1}_{i,j,k}-q^{n+1}_{i,j,k-1}\right)}{\Delta z^{n+1}_{i,j,k-1/2}}\right]=\frac{\tilde{u}^{n+1}_{i+1/2,j,k}\Delta z^{n+1}_{i+1/2,j,k}-\tilde{u}^{n+1}_{i-1/2,j,k}\Delta z^{n+1}_{i-1/2,j,k}}{\Delta x}+ \quad (6.12)$$
$$+\frac{\tilde{v}^{n+1}_{i,j+1/2,k}\Delta z^{n+1}_{i,j+1/2,k}-\tilde{v}^{n+1}_{i,j-1/2,k}\Delta z^{n+1}_{i,j-1/2,k}}{\Delta y}+\tilde{w}^{n+1}_{i,j,k+1/2}-\tilde{w}^{n+1}_{i,j,k-1/2}$$

that can be solved iteratively using the preconditioned conjugate gradient method. In equation (6.12) $\tilde{u}$, $\tilde{v}$ and $\tilde{w}$ are the velocity components obtained after the first computational step; N_x, N_y, and N_z are the number of computational cells in each direction, and Δx, Δy and Δz_k are the dimensions of each cell. The final velocity components are found by correcting the provisional velocity field with the gradient of the hydrodynamic velocity:

$$u^{n+1}_{i+1/2,j,k}=\tilde{u}^{n+1}_{i+1/2,j,k}-\frac{\Delta t}{\Delta x}\left(q^{n+1}_{i+1,j,k}-q^{n+1}_{i,j,k}\right) \quad (6.13)$$

$$v^{n+1}_{i,j+1/2,k}=\tilde{v}^{n+1}_{i,j+1/2,k}-\frac{\Delta t}{\Delta y}\left(q^{n+1}_{i,j+1,k}-q^{n+1}_{i,j,k}\right) \quad (6.14)$$

$$w^{n+1}_{i,j,k+1/2}=\tilde{w}^{n+1}_{i,j,k+1/2}-\frac{\Delta t}{\Delta z^{n+1}_{i,j,k+1/2}}\left(q^{n+1}_{i,j,k+1}-q^{n+1}_{i,j,k}\right) \quad (6.15)$$

6.3.3 Modelled cases

Several cases were considered for modelling, corresponding to different typical local wind conditions, measured during persistent wind events. The characteristic wind parameters used for each are specified below. The values of the wind and river flow characteristics are taken as the average over the period during which the field measurements were done (typically between 8:00 AM and 8:00 PM) for cases A and B; for case C, the average is done over the 12 hours previous to the time at which the satellite image was taken.

The computational domain considered was limited by the coastline, the 600 m isobath, a northern transect off Cape Salou, and a southern transect at the Columbretes Islands. The computational grid consisted of 336x200 cells, with a characteristic cell size of 150.6m x 153m. The underlying mesoscale circulation in the region was not included, and the only driving mechanisms considered for the hydrodynamics simulations were the river discharge momentum and the wind.

6.3.3.1 Case A (PIONEER II)

Test case A is based on measurements taken on July 11th, 1999 at over 150 stations at and near the Ebre river mouth. These measurements included salinity and nutrient concentration at the free surface, and occasional vertical profiles of these parameters. The mean wind observed throughout the day presented a slightly southeastern component (97.2º clockwise from the north), with a 3.8 m/s speed. The dispersion in both variables was 10.6º and 0.5 m/s, respectively. The mean river discharge was 112.8 m^3/s.

Surface values for salinity and temperature were taken at a number of stations on the north hemidelta, following the freshwater plume. In addition, vertical profiles, and water samples at different depths, were obtained at seven sea stations, including four near the rivermouth. Both the surface measurement points and the sea stations are shown in figure 6.18:

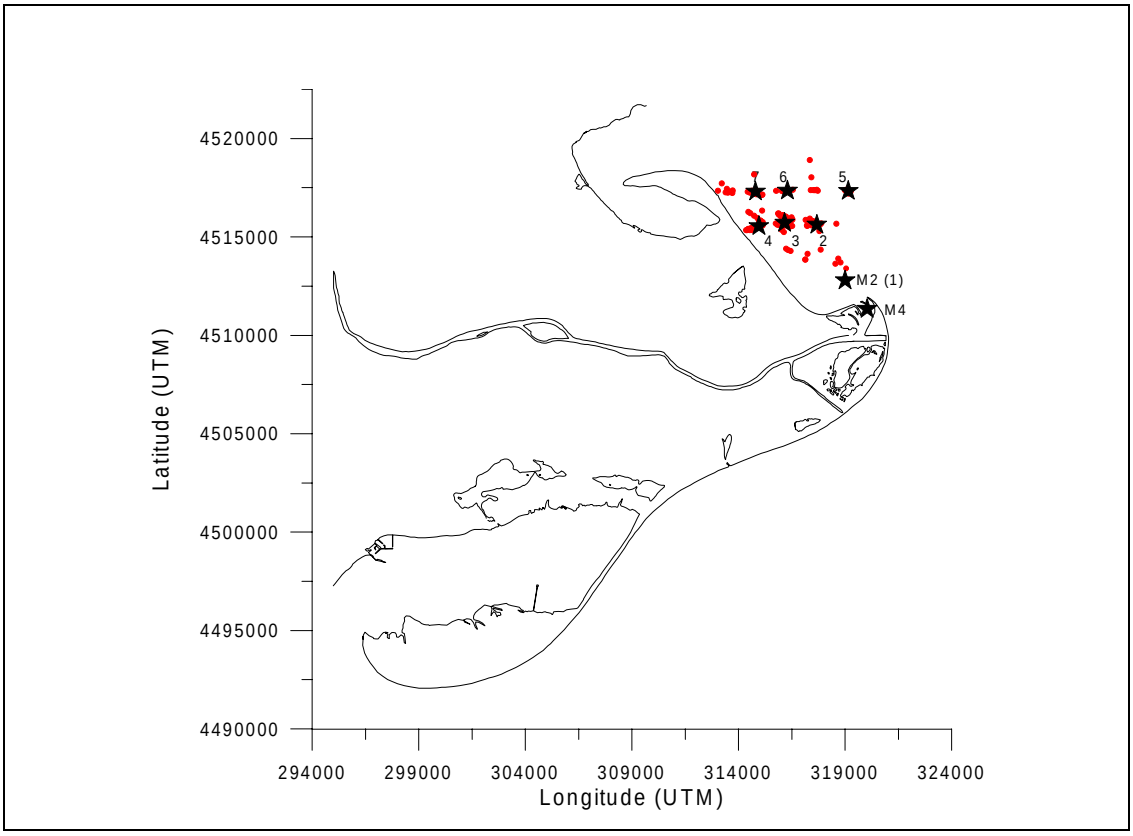

Figure 6.18: Measuring stations at the Ebre delta during July 11th, 1999. The stars (★) show the measuring points used for comparison with modelled data.

The hydrodynamic field existing in the area was modelled using the numerical model described above, furnished with the corresponding meteorological and river discharge data. After the stationary state is reached, the current field near the river mouth shows a characteristic westward pattern, deflecting the river discharge shortly after it has entered the coastal waters, and turning north further along the coast, following the bottom topography (figures 6.19 and 6.20). The circulation along the eastern coast of the delta appears to be, however, mainly southwards.

Parameter	Value
River discharge (m^3/s)	112.8
Wind speed (m/s)	3.8
Wind direction (º)	97.2
Total simulation time (hrs)	235.2
Computational timestep (s)	70.0
Horizontal viscosity coeff.	80.0

Table 6.1: Computational parameters used in the TRIM3D model for case A.

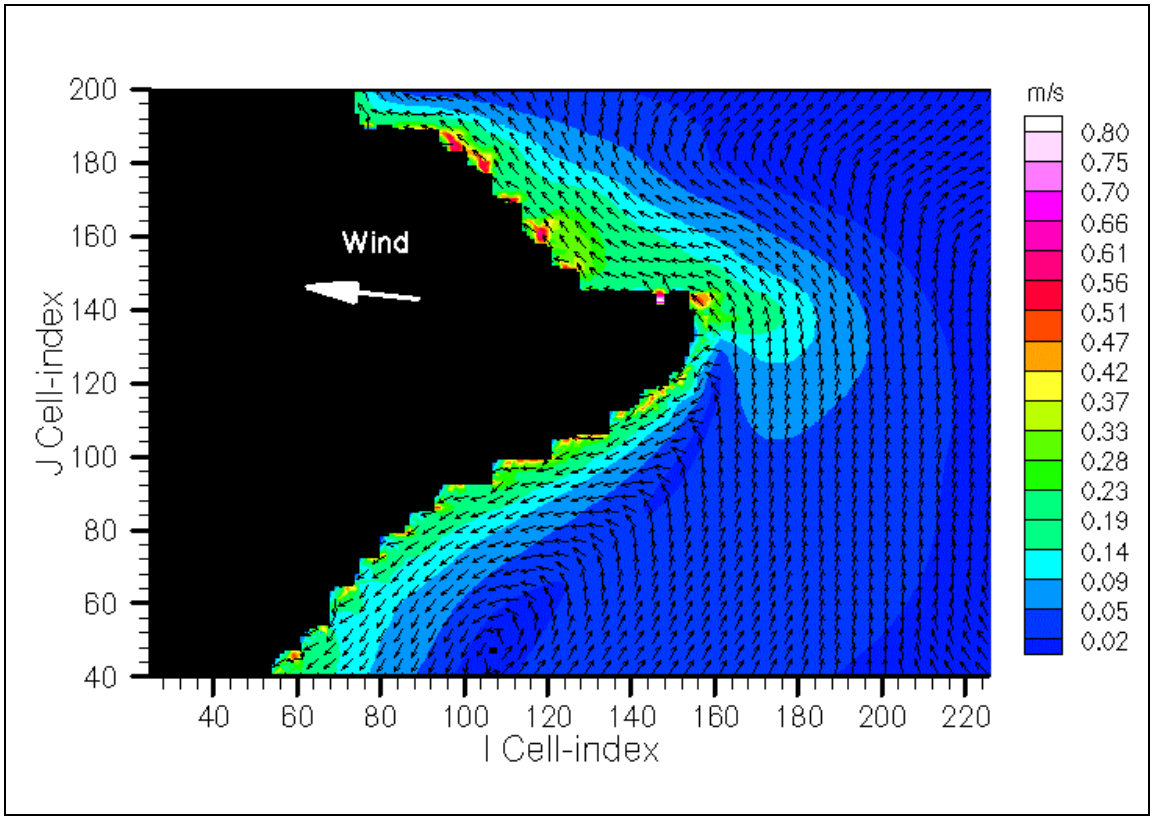

Figure 6.19: Current field induced by a wind blowing from the ESE, near the Ebre river mouth. Axes units must be multiplied by 150.6 (X) and 153 (Y) to yield distances in meters.

The evolution of the river plume was modelled using the freshwater discharge rate given in table 6.1. The most relevant transport parameters used in the numerical transport modelling are summarised in table 6.2; the total simulation time was approximately 10 hours, with a computational timestep of 0.7 sec, and the total number of particles within the waterbody at the end of the simulation was about 48,000. The dispersion coefficients were computed following Elder's (1959) expression (equation 2.159), with the constants shown in table 6.2; it was assumed that freshwater transport occured only in the upper layer of the watercolumn (upper 1m), and that the velocity profile within this layer was uniform. The particle cloud resulting from the simulation is shown in figure 6.21, whereas figure 6.22 presents the salinity distribution obtained from the set of particles using the BC method.

Parameter	Value
Total simulation time (hrs)	9.33
Computational timestep (sec)	0.70
c_L (Longitudinal dispersion constant)	950.9
c_T (Lateral dispersion constant)	750.0
c_V (Vertical dispersion constant)	0.16
Final number of particles	48,000

Table 6.2: Parameters used in the LIMMIX model run corresponding to case A.

The modelled particle cloud was used to obtain salinity values at a series of locations where field measurements were available, which are highlighted with a ★ symbol in figure 6.18. The coordinates of these points, together with the measured salinity, are given in table 6.3.

	X (UTM)	Y (UTM)	Salinity (ppt)
M4	320038.9	4511345.3	23.87
M2 (1)	319002.5	4512791.3	18.05
2	314951.0	4515545.3	27.65
3	316167.3	4515722.3	26.54
4	319152.8	4517333.3	28.13
5	317672.5	4515623.3	32.22
6	314799.5	4517309.3	26.40
7	316296.4	4517348.3	28.41

Table 6.3: Measuring stations used in the comparison with modelled data.

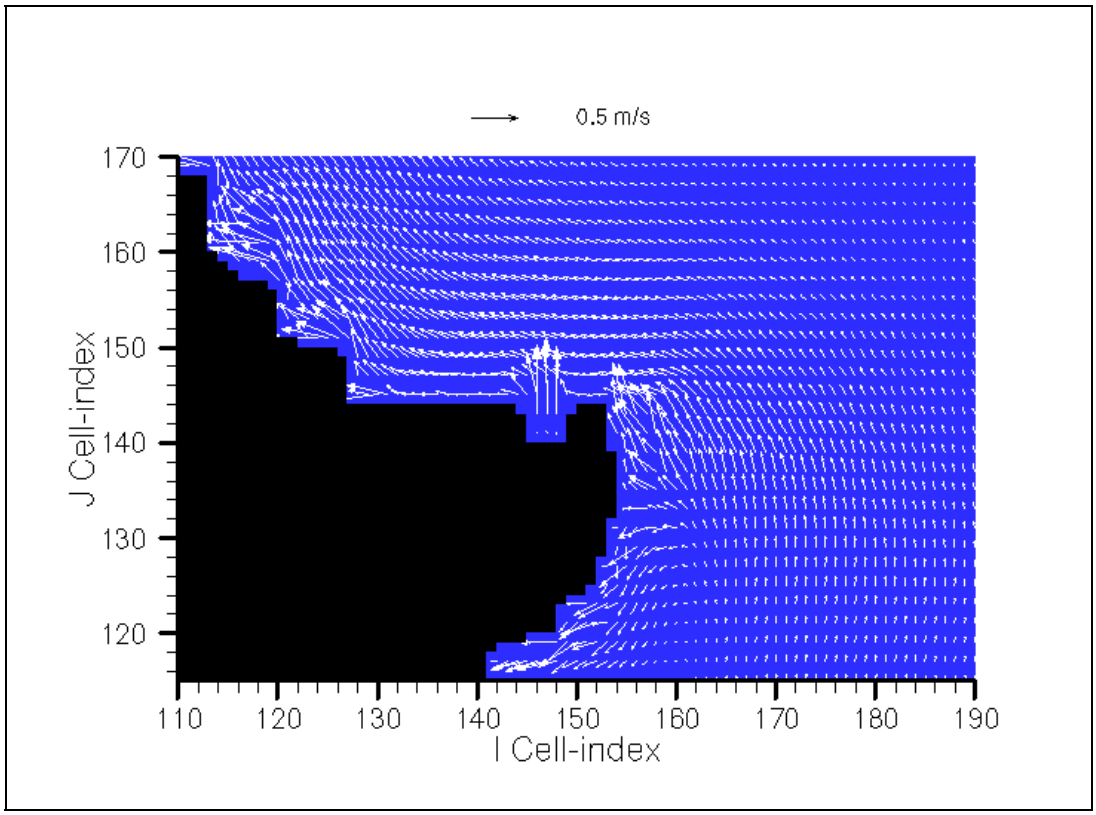

Figure 6.20: Close-up of the current field induced by a wind blowing from the ESE, near the Ebre river mouth. Axes units must be multiplied by 150.6 (X) and 153 (Y) to yield distances in meters.

The conversion from discrete particle positions to salinity values was performed using the BC method, and a wide range of integration volumes was scanned in order to find the one which adjusted best to the field data. The comparison between measured and modelled data is shown in figure 6.23; the selected points correspond to measuring stations where vertical profiles were obtained, and the surface salinity only is used here. It can be seen that the agreement between the modelled values and those measured during the field campaign is satisfactory at most of the measuring stations, although the adjustment tends to be not as good at the front of the plume, perhaps because of the scarcity of particle positions in this area, and closest to the river mouth, probably due to the effects of a large integration volume. This latter argument is reinforced by the fact that smaller integration volumes lead to a better agreement at station M2, but increase the error obtained at the rest of locations (figure 6.24). The influence of the integration volume on the results is shown in figure 6.25, in which an estimation of the mean relative error, computed following equation (6.16), is plotted against the horizontal dimensions of the volume of integration, keeping the vertical dimension constant.

$$\text{Error} = \frac{1}{N}\sum_{i=1}^{N}\frac{\left|S^{i}_{\text{Measured}} - S^{i}_{\text{Computed}}\right|}{S^{i}_{\text{Measured}}} \qquad (6.16)$$

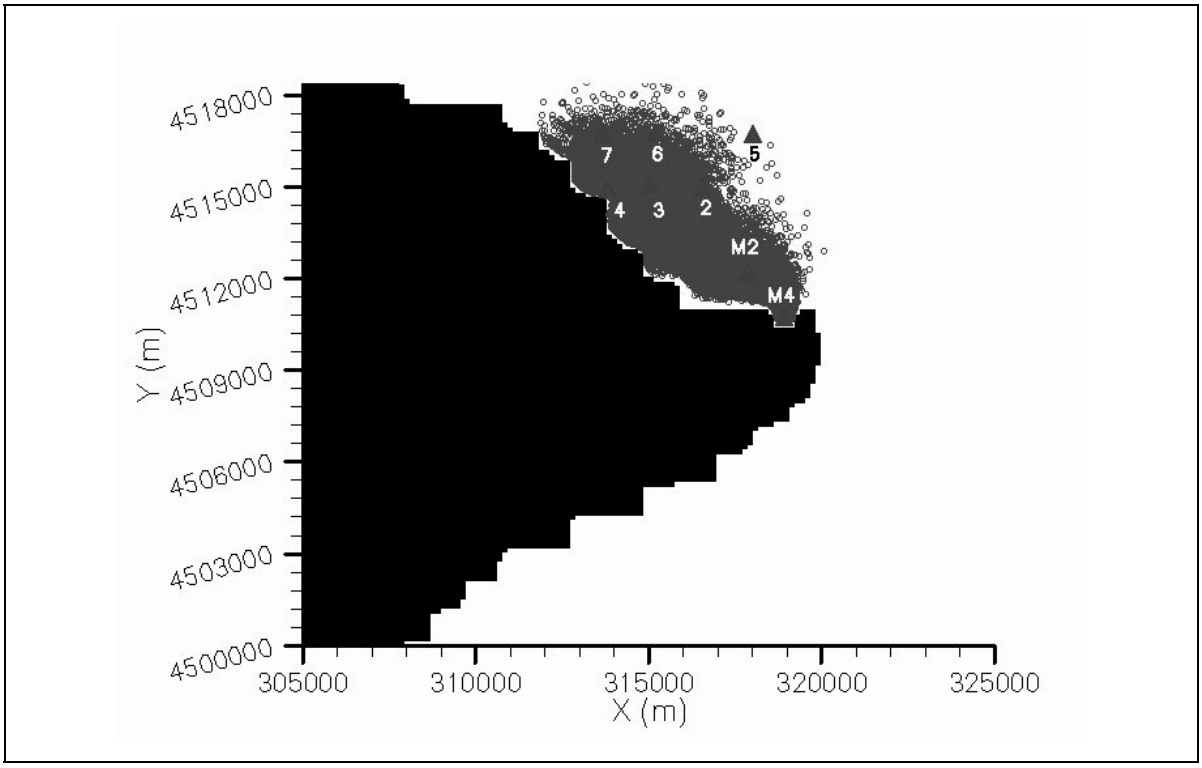

Figure 6.21: Particle cloud resulting from the simulation of the Ebre river plume, corresponding to case A.

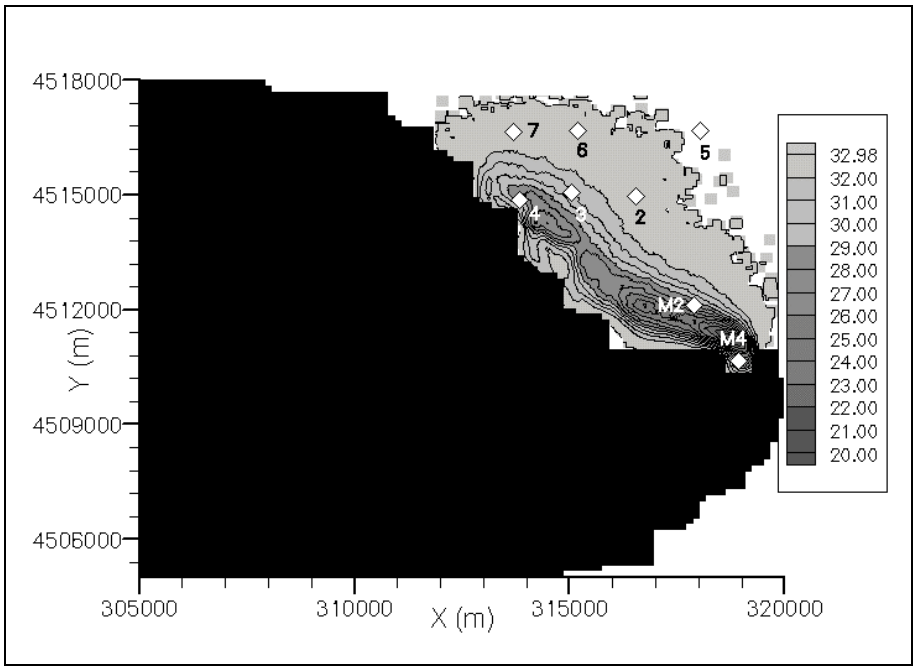

Figure 6.22: Salinity contours for the river Ebre plume, corresponding to case A, with Q = 112.8 m^3/s.

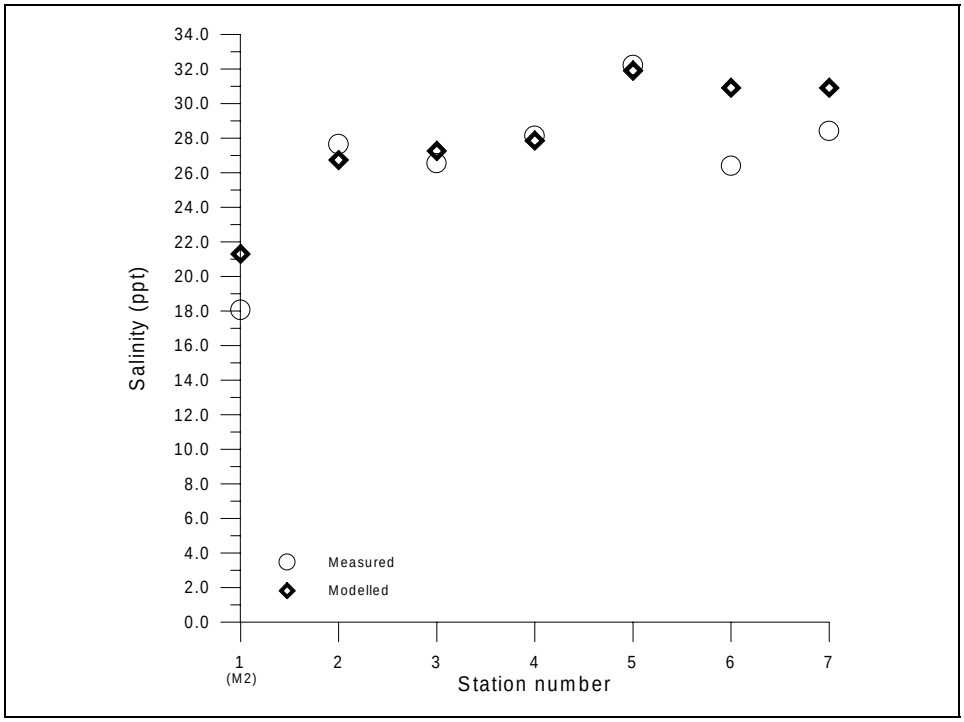

Figure 6.23: Measured and modelled salinity values at the positions given in table 6.3. The modelled values have been computed using the BC method with a 6,000mx6,000mx10m integration volume.

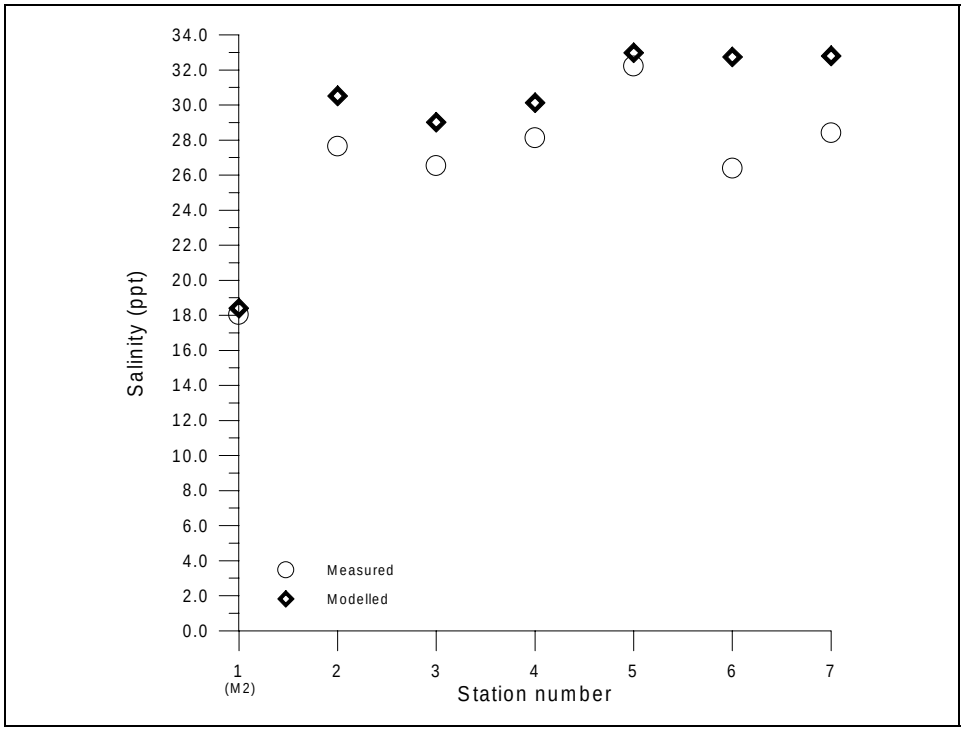

Figure 6.24: Measured and modelled salinity values at the positions given in table 6.3. The modelled values have been computed using the BC method with a 3,000mx3,000mx10m integration volume.

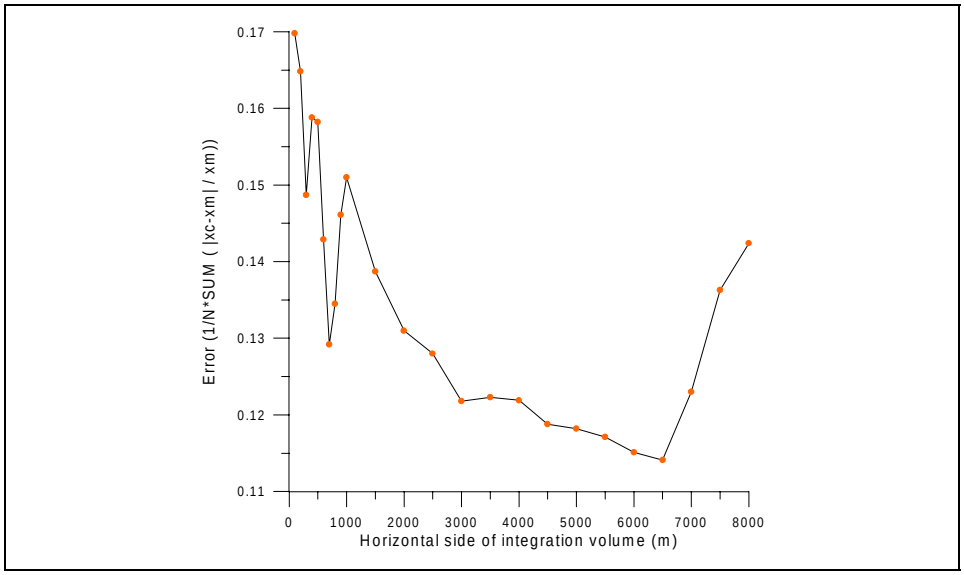

Figure 6.25: Computed error as a function of integration volume, calculated using equation 6.16.

The relationship between measured and modelled salinity values at all the measuring stations has also been obtained, using the SPH method with different integration lengths. Figure 6.26 shows the data found using a 5,000 m integration length, and it can be seen that a large scatter exists in the modelled salinity, although there is not a clear under- or over-estimation of the salinity values. The mean relative error in this case is 0.12.

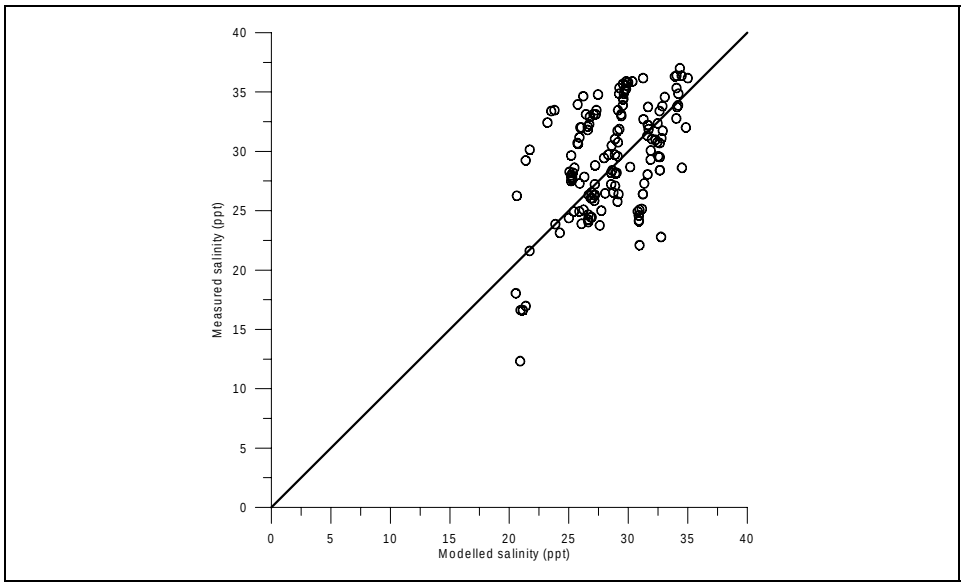

Figure 6.26: Measured *vs* modelled salinity for all the measuring stations in figure 6.18. The modelled salinity has been computed using the SPH mapping method with a 5,000m integration length.

In order to compare the influence of the river outflow on the local hydrodynamics, an additional run of the TRIM3D model was performed, significantly increasing the value of the river discharge. Using the same model parameters as for the previous case (defined in table 6.1), but taking Q = 1400 m^3/s, the resulting circulation pattern near the river mouth differs considerably from that obtained for a smaller Q, although the general hydrodynamic circulation away from this region remains controlled by the effects of the wind (figure 6.27).

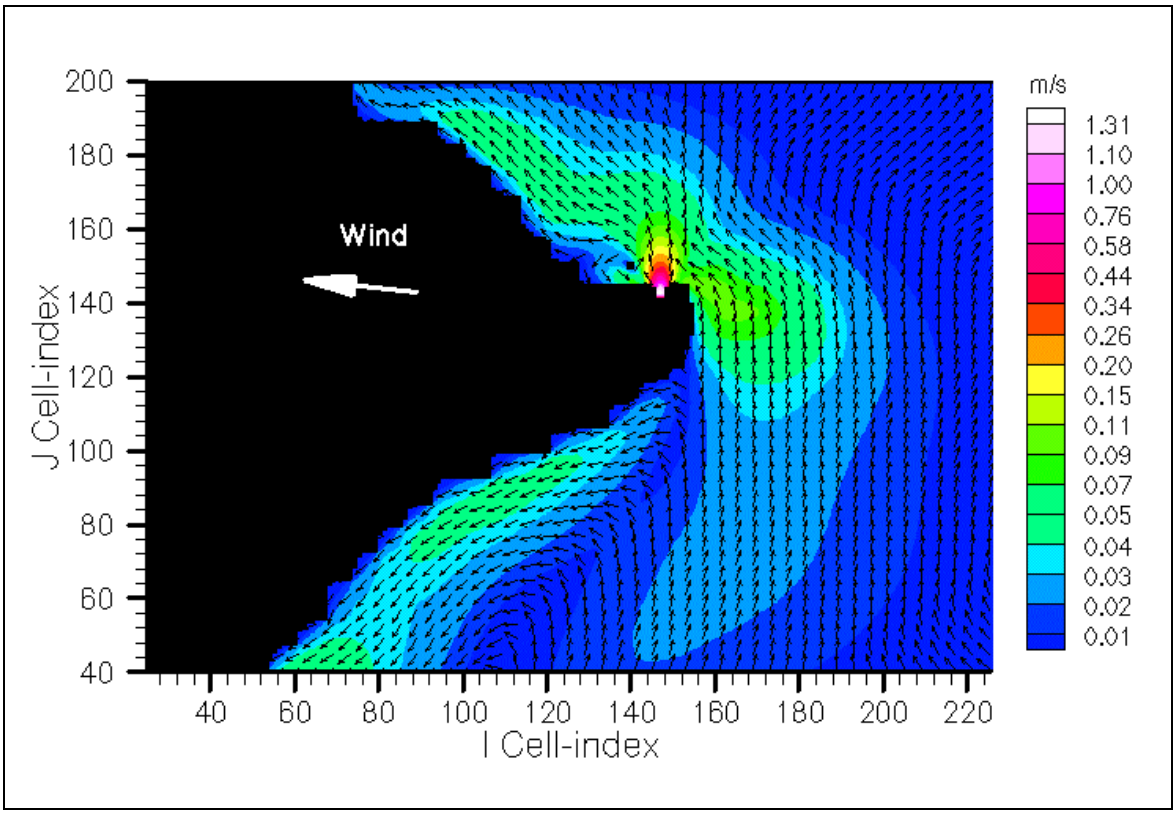

Figure 6.27: Current field induced by a wind blowing from the ESE, near the Ebre river mouth, for Q = 1400 m^3/s. Axes units must be multiplied by 150.6 (X) and 153 (Y) to yield distances in meters.

The effects of the river discharge momentum are clearly seen in figure 6.28, which is a close-up of the hydrodynamics near the river mouth. The outflow velocity is larger than that in the previous case, and it reaches further out into the sea, deflecting the wind-induced circulation; a cyclonic eddy appears on the western side of the freshwater jet, due to the interaction between the river discharge and the currents induced by the wind.

Under these conditions, the river plume is expected to extend further out into the sea, instead of following the north coast of the delta as in the previous case. The simulation of the freshwater transport, using the parameters given in table 6.2, yields this predicted behaviour, as becomes evident in figures 6.29 and 6.30, which show the cloud of discrete particles generated by the LIMMIX run, and the salinity distribution obtained using the BC method.

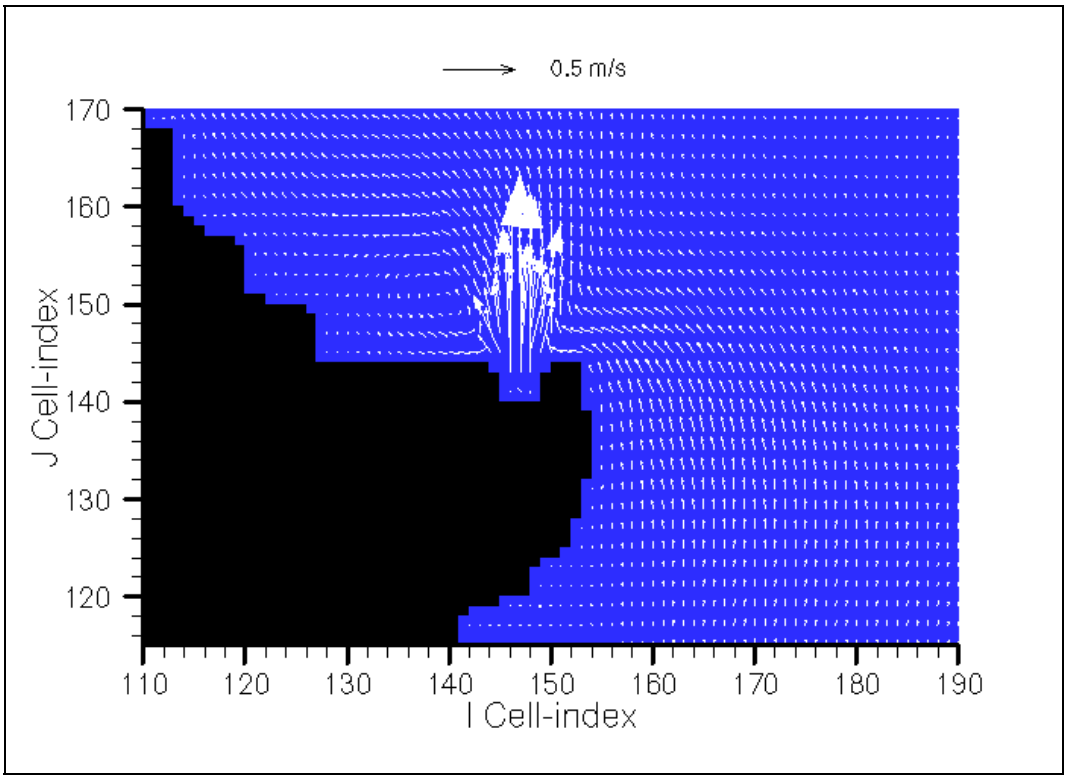

Figure 6.28: Close-up of the current field induced by a wind blowing from the ESE, near the Ebre river mouth, for Q = 1,400 m^3/s. Axes units must be multiplied by 150.6 (X) and 153 (Y) to yield distances in meters.

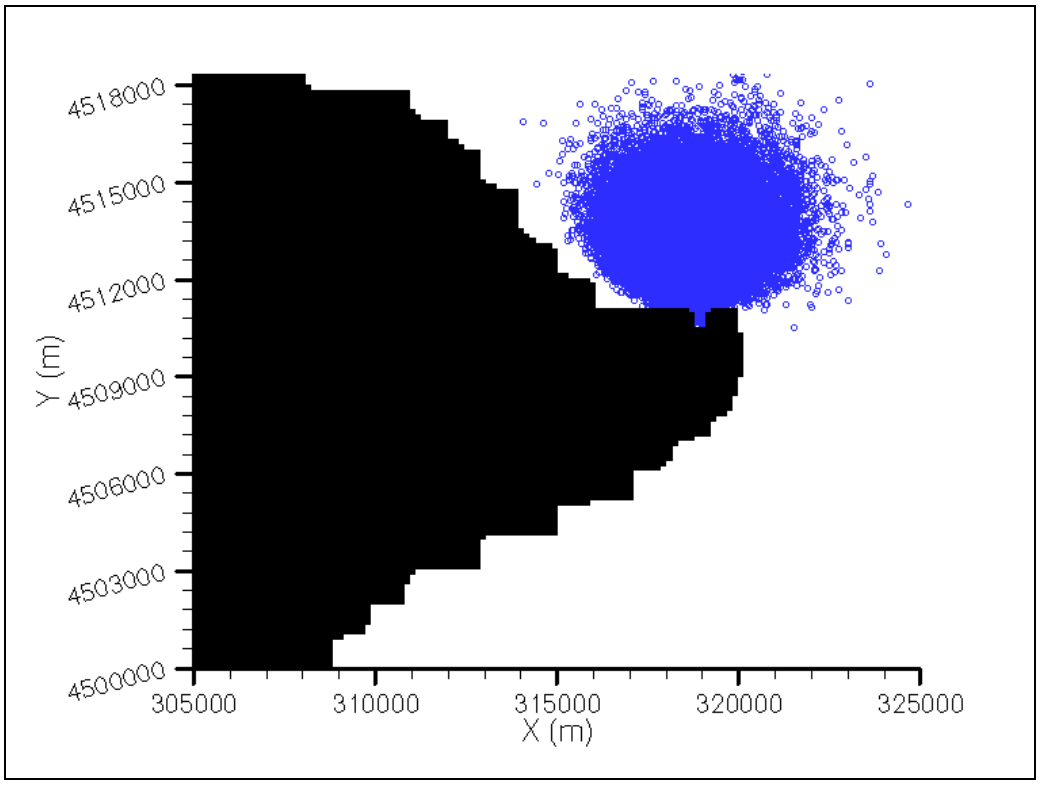

Figure 6.29: Particle cloud resulting from the simulation of the Ebre river plume, corresponding to case A, but with Q = 1,400 m^3/s.

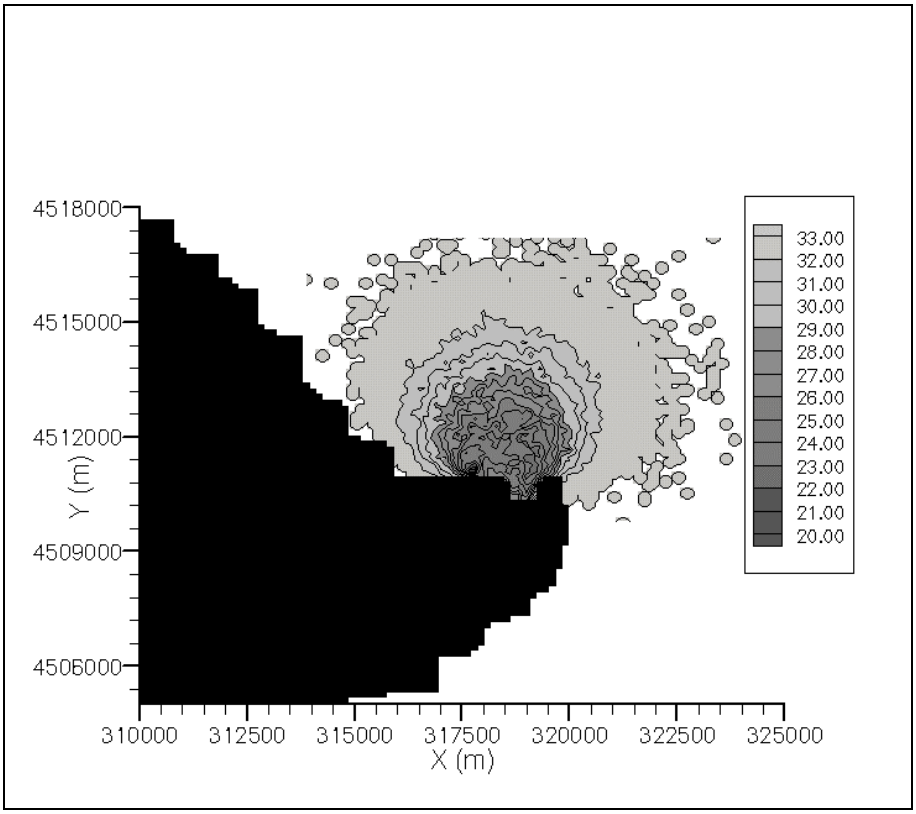

Figure 6.30: Salinity contours for the river Ebre plume, corresponding to case A, but with Q = 1,400 m^3/s.

Therefore, it appears that the main driving mechanism for the circulation near the mouth of the Ebre river depends on the magnitude of the river flow. For typical river discharge rates (≤ 300 m^3/s), the currents and, consequently, the river plume, are controlled mainly by the prevailing wind field, whereas for larger values of the freshwater flow (~ 1400 m^3/s) the governing role is played by the momentum of the river discharge.

6.3.3.2 Case B (PIONEER IV)

The salinity and water temperature measurements taken on February 4th, 2000 at about 55 different locations (figure 6.31) in front of the river mouth were used as a second test case to estimate the capabilities of the transport model. The mean values of the wind velocity and direction observed during that day were 2.2 m/s and 189.7º (clockwise from the north), respectively, whilst the dispersion in these variables was estimated to be 0.9 m/s and 97.8º. The mean river discharge for this date was somewhat higher than for case A, 166.6 m^3/s, due to the winter conditions.

The hydrodynamic field induced by the river discharge and the prevailing wind was again modelled with TRIM-3D, using the parameters given in the table below (6.4). Under stationary conditions, the resulting currents follow a western direction in the region near the river mouth, where the freshwater discharge is rapidly deflected, and then follow the isobaths to the north, along the coast. The interaction of the river flow and the coastal wind-induced currents generates a small cyclonic gyre immediately to the west of the river mouth. Away from the influence of the river discharge, the modelled flow is purely wind-driven, following the bathymetric contours (figures 6.32 and 6.33).

Parameter	Value
River discharge (m^3/s)	166.6
Wind speed (m/s)	2.2
Wind direction (º)	189.7
Total simulation time (hrs)	336.0
Computational timestep (s)	100.0
Horizontal viscosity coeff.	50.0

Table 6.4: Computational parameters used in the TRIM3D model for case B.

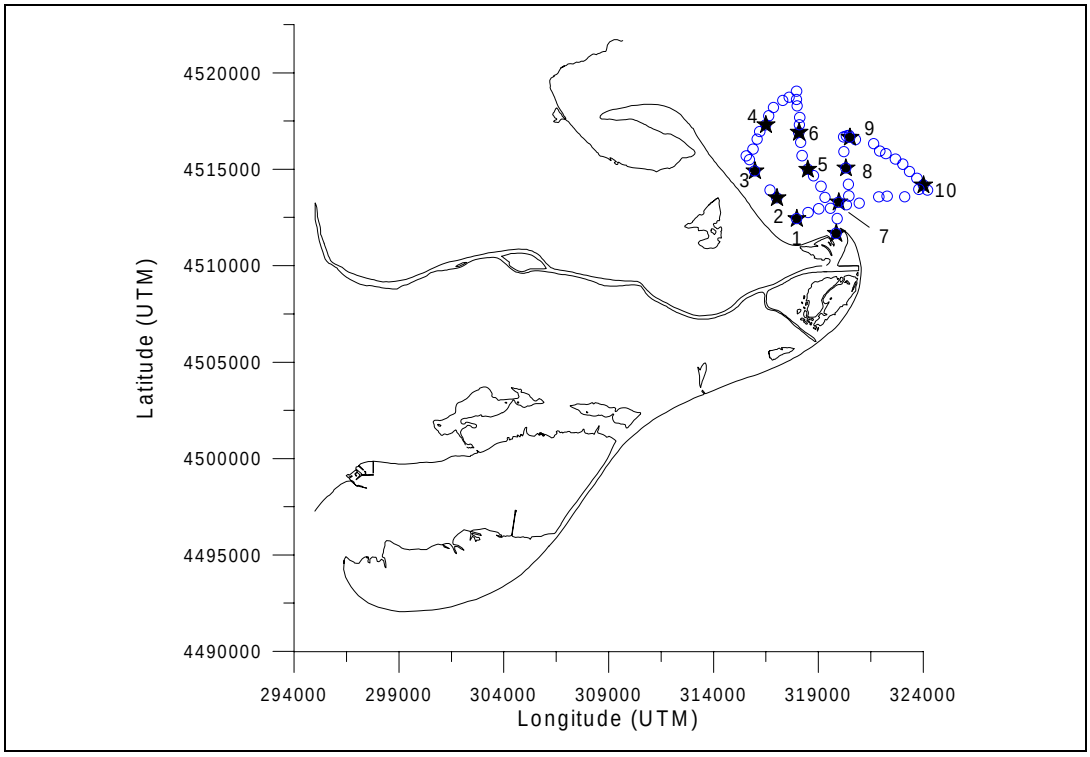

Figure 6.31: Position of the sampling stations near the river mouth (February 4th, 2000).

The river discharge rate listed in table 6.4 was used to model the behaviour of the river plume. Table 6.5 presents the relevant transport parameters used in the dispersion model run; the total simulation time was just over 22 hours, with a numerical timestep of 1.5 sec; and the final number of particles within the simulation was 53,334. The resulting particle cloud is shown in figure 6.34.

Parameter	Value
Total simulation time (hrs)	22.2
Computational timestep (sec)	1.50
c_L (Longitudinal dispersion constant)	750.9
c_T (Lateral dispersion constant)	750.0
c_V (Vertical dispersion constant)	0.16
Final number of particles	53,334

Table 6.5: Parameters used in the LIMMIX model run corresponding to case B.

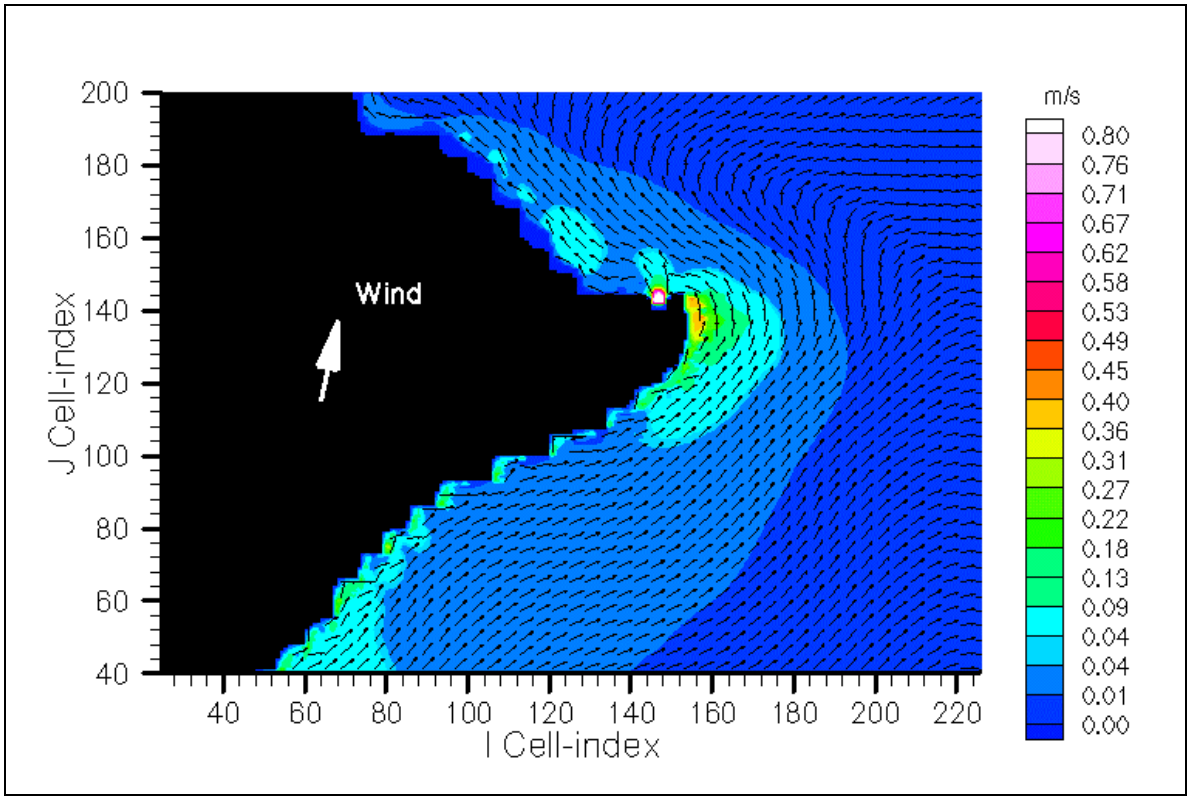

Figure 6.32: Current field induced by a wind blowing from the S, near the Ebre river mouth. Distances in meters are found multiplying by 150.6 (X) and 153 (Y).

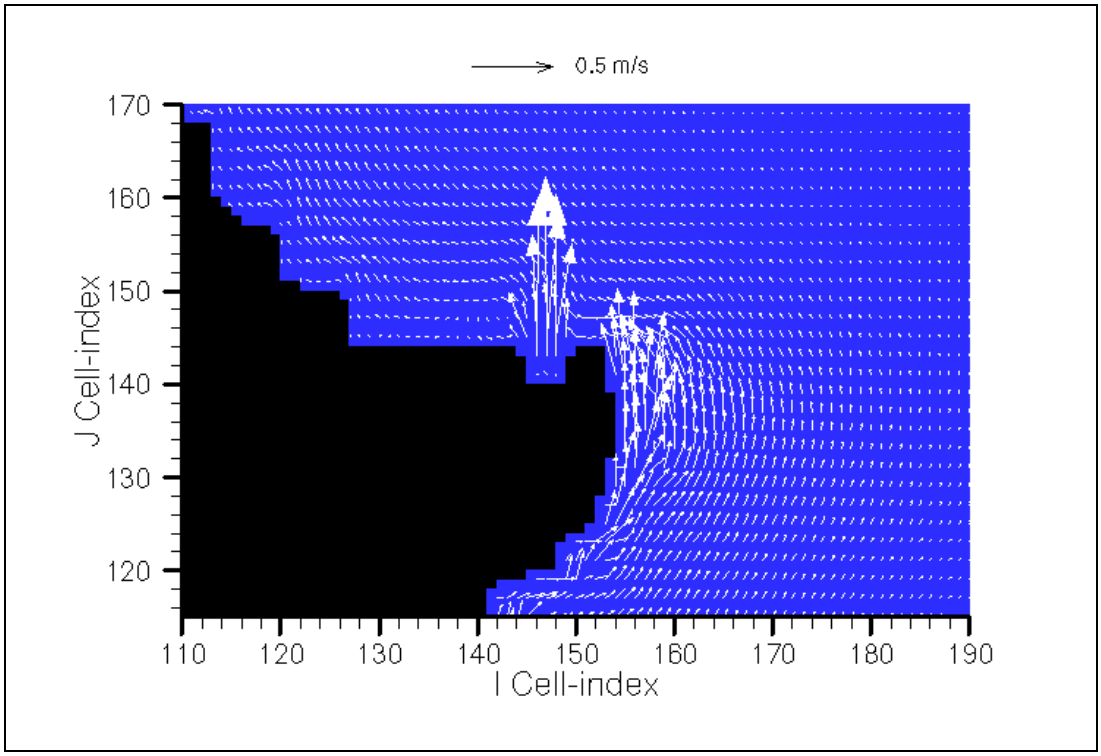

Figure 6.33: Close-up of the current field induced by a wind blowing from the South, near the Ebre river mouth. Axes must be multiplied by 150.6 (X) and 153 (Y) to yield distances in meters.

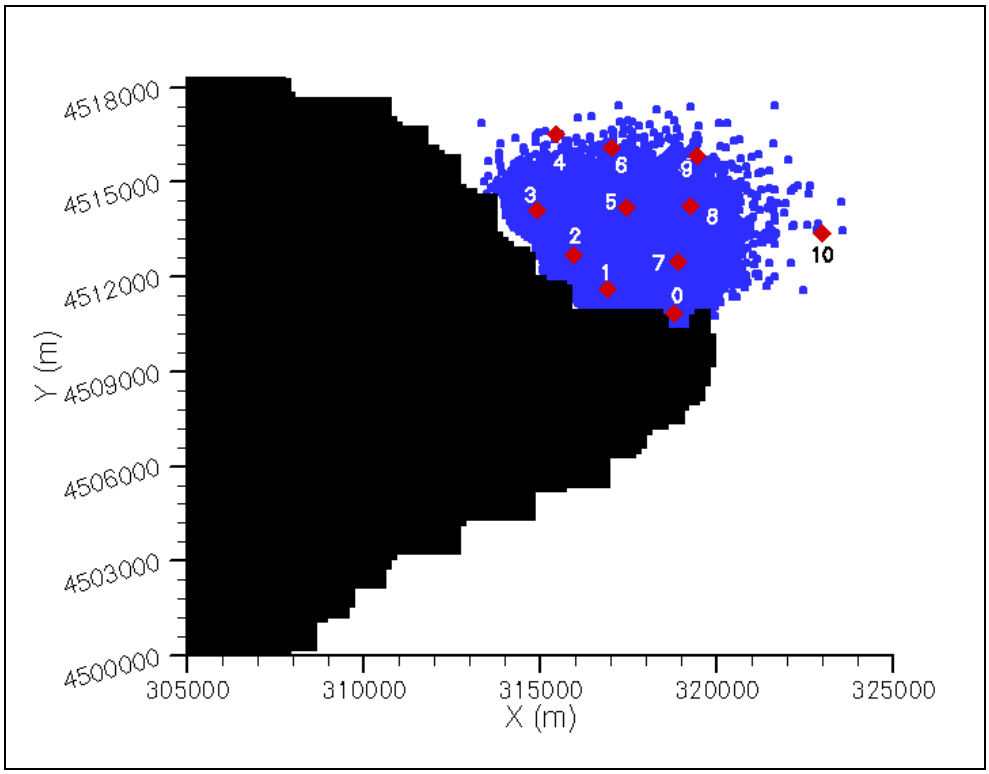

Figure 6.34: Particle cloud resulting from the simulation of the Ebre river plume, corresponding to case B.

From the resulting particle cloud, salinity values were obtained at a number of locations, marked in figure 6.31 with a star symbol, the coordinates of which are given in table 6.6.

	X (UTM)	Y (UTM)	Salinity (ppt)
0	319853.6	4511663	0.75
1	317971.3	4512431	4.79
2	317026.2	4513510	3.45
3	315976	4514911	4.96
4	316500.7	4517300	31.81
5	318498.7	4514992	19.00
6	318081.3	4516909	21.22
7	319977.7	4513290	20.15
8	320316.3	4515059	21.37
9	320509.6	4516646	29.45
10	324011.4	4514174	26.80

Table 6.6: Measure stations used in the comparison with modelled data.

In this case, the transformation from the discrete particle distribution to the values of salinity was done using both the BC and the SPH methods. As in test case A, a wide range of integration lengths was used in order to find the one which yields best data fitting, and it was found that the optimal length depends on the method employed. The measured and the modelled salinity are shown in figures 6.35 and 6.36, for the BC and SPH mapping method, respectively. It can be seen that the SPH method appears to be somewhat more accurate than the BC method, although for both algorithms some of the modelled values present very large differences in relation to the measured salinity. This can be partly explained by the particular distribution of the measured salinity, which is evident in

figure 6.39a. Although a salinity increase with the distance to the river mouth is expected, as a general trend, it can be seen that the measured values of salinity are high near the river mouth, while lower salinities are observed farther away; on the other hand, the salinity distribution obtained from the numerical model does follow the expected trend (figure 6.39b). This fact suggests that some kind of error occurred during the acquisition or water sample processing phase, or that additional transport mechanisms which are not included in the transport model were acting on the freshwater plume. This is likely to be because of the difficulty in defining a single integration length that is suitable for all the test points.

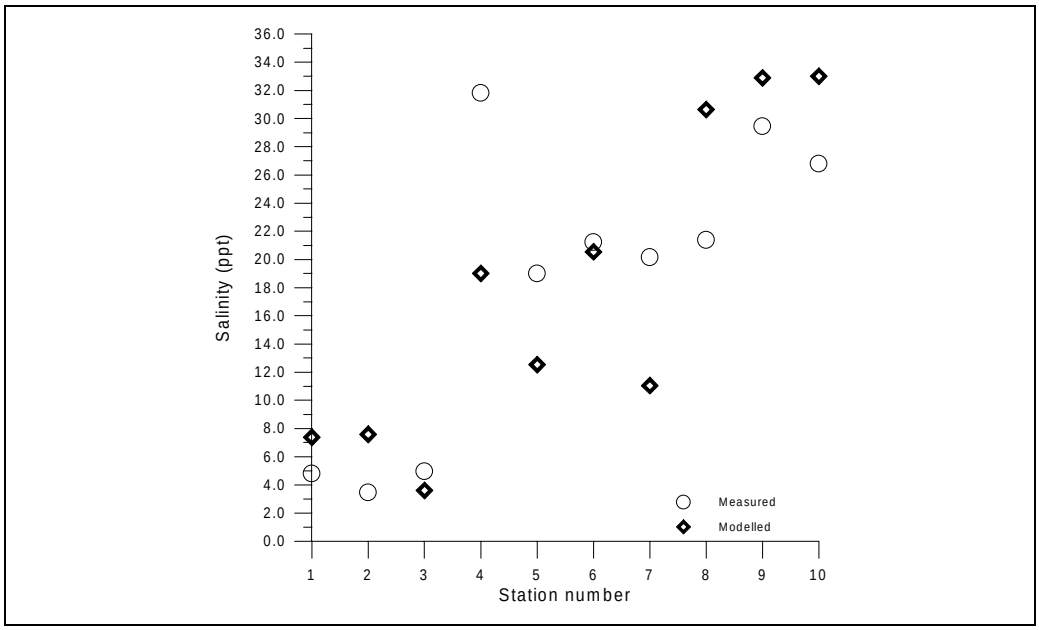

Figure 6.35: Measured and modelled salinity values at the positions given in table 6.6. The modelled values have been computed using the BC method with a 3,500mx3,500mx10m integration volume.

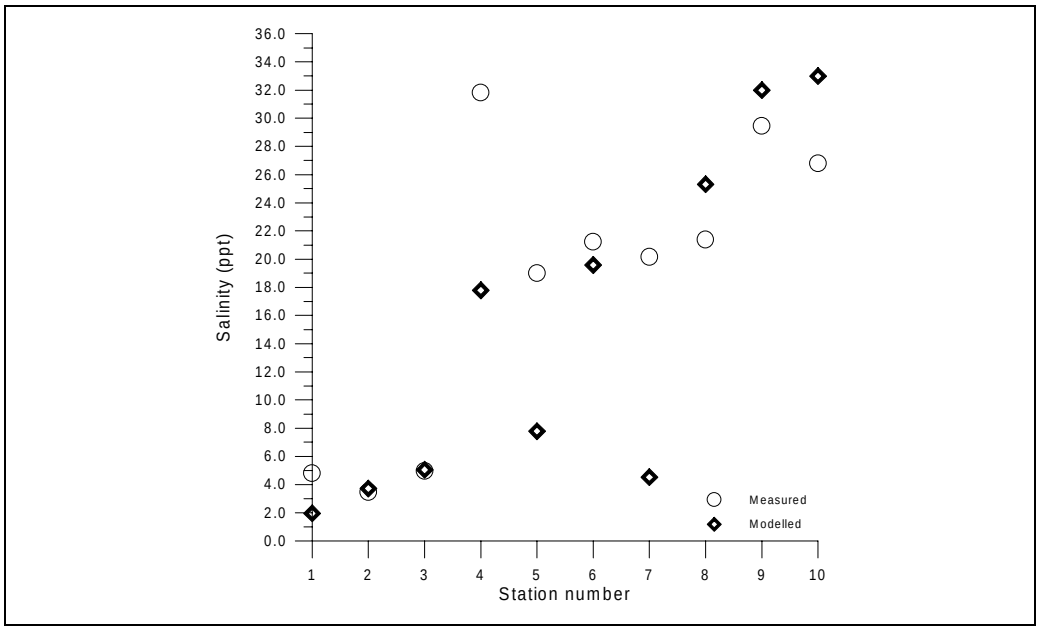

Figure 6.36: Measured and modelled salinity values at the positions given in table 6.6. The modelled values have been computed using the SPH method with a 2,500m integration length.

An estimation of the error in the data fitting as a function of the integration length was done using equation 6.16, for both methods. Figures 6.37 and 6.38 show the rmae error obtained, where it is clear that the optimal integration length differs for the BC and the SPH method.

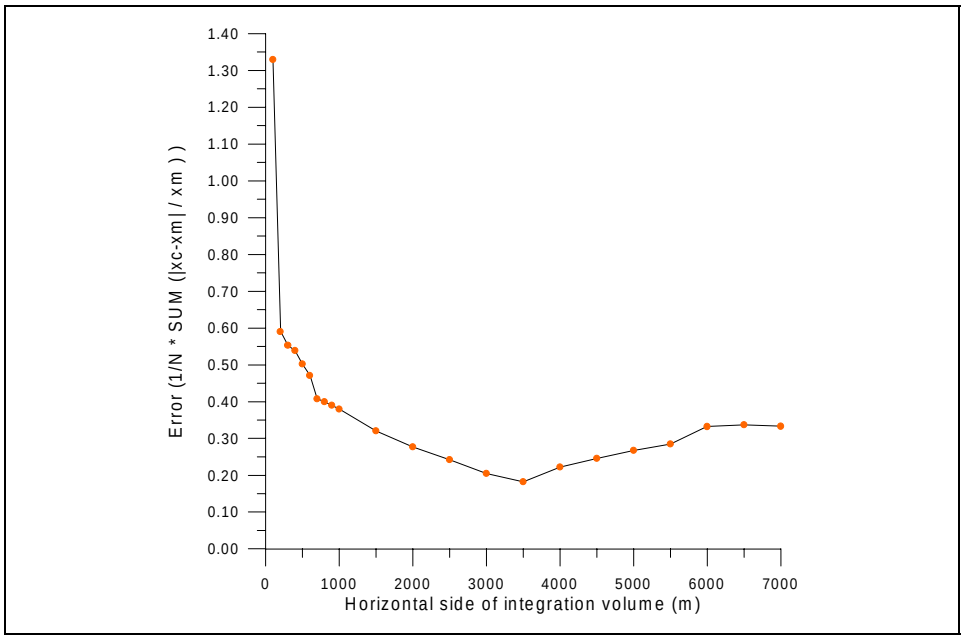

Figure 6.37: Rmae error computed as a function of the integration volume, for the BC method, computed using equation 6.16.

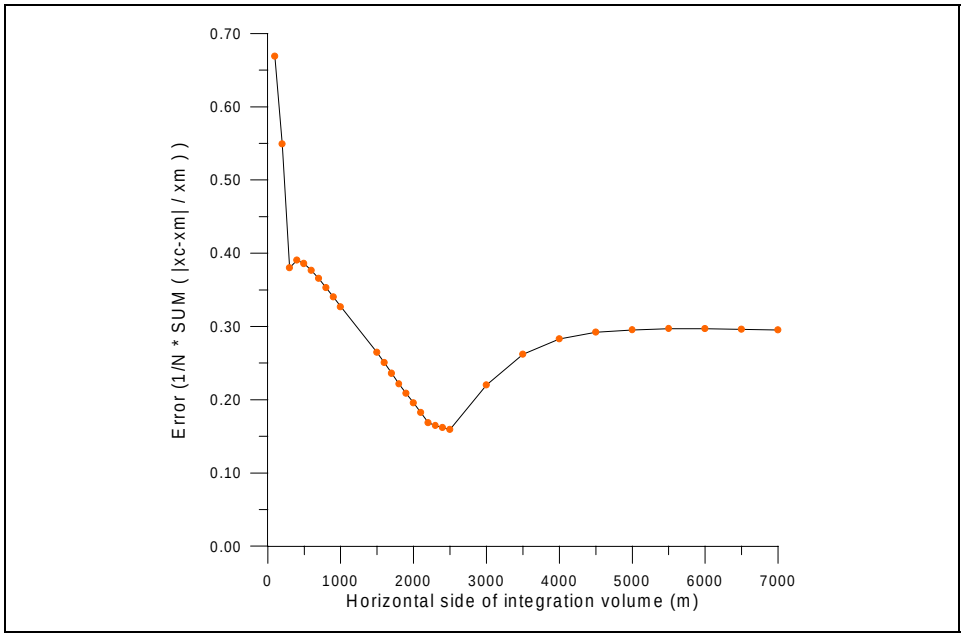

Figure 6.38: Rmae error computed as a function of the integration volume, for the SPH method, computed using equation 6.16.

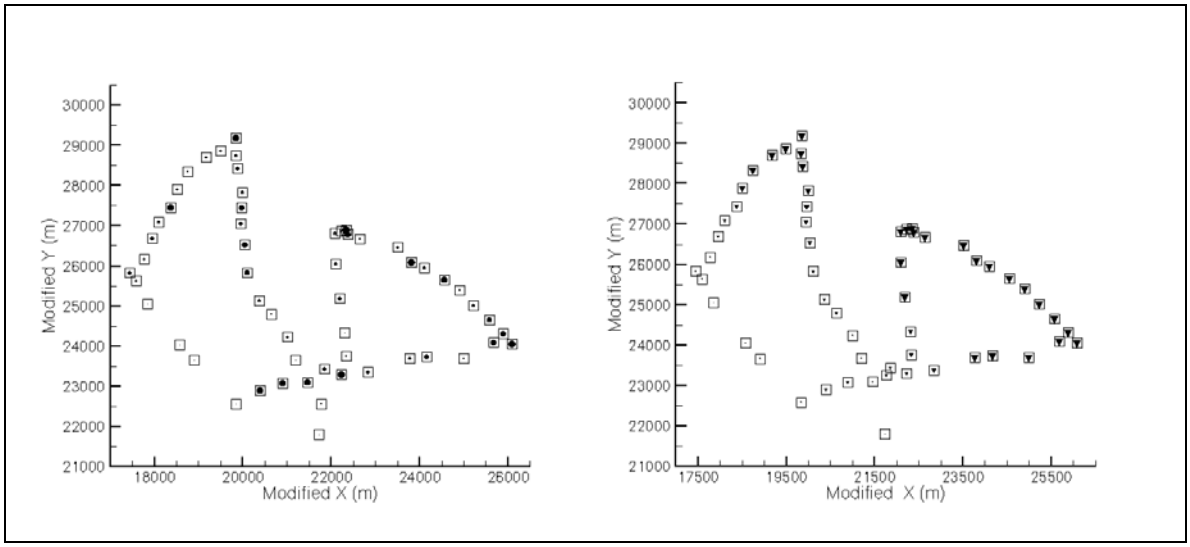

Figure 6.39: Measured (left) and modelled (right) salinities at all stations for case B. The squares mark the position of the measuring station, and the size of the inset symbol is proportional to the salinity at that point. The square closest to the X-axis corresponds to the river mouth (station 0 in table 6.6).

The river plume in both simulated cases extends towards the northern half of the delta, due to the currents induced by predominantly southern and eastern winds, when the freshwater flow rate is of the order of 100-200 m^3/s. Under flood conditions, i.e., when the river discharge is larger than about 1,000 m^3/s, the influence of the wind on the circulation near the river mouth is much smaller, and the momentum of the freshwater becomes the main current-inducing mechanism. For winds blowing from the North and the West, the hydrodynamic currents under normal river conditions tend to drag the freshwater plume along the coast of the delta in a general southern direction, sometimes detaching it from the shallower waters and taking it into the open sea. The lack of measured salinity data under these wind conditions does not allow a quantitative comparison of model results with field measurements; however, a qualitative comparison has been attempted using a plume image taken by a satellite.

6.3.3.3 Case C (Satellite image)

A third case was defined in order to compare, in a qualitative manner, the modelled freshwater plume with the plume observed by remote sensing procedures. A SPOT satellite image (figure 6.40) corresponding to July 6th, 1997, was chosen, and the contours of the river plume were digitised to compare with the modelled particle distribution.

These satellite data correspond to extra-atmospheric radiances in the red SPOT XS2 band centred at 650 nm. In that channel, radiances are strongly dependent on the concentration of fine suspended particulate matter in the Ebre river plume (Ouillon, 2002). The patterns of concentration are similar to those of salinity when the plume is stratified, as was the case in July 1997.

The hydrodynamic field at the Ebre delta area was computed using the TRIM-3D model, and the mean meteorological data measured on July 6th, 1997, together with the mean river discharge flow on that day. The parameters used in the TRIM-3D model run are given in table 6.7, and the resulting hydrodynamic pattern is shown in figure 6.41.

Figure 6.40: Satellite image of the river Ebre's freshwater plume, on July 6th, 1997, at 11:03 UTM. The colour scale refers to extra-atmospheric radiances measured by SPOT, HRV sensor, XS2 channel ((c) CNES).

Parameter	Value
River discharge (m^3/s)	149.4
Wind speed (m/s)	4.63
Wind direction (º)	335.1
Total simulation time (hrs)	336.0
Computational timestep (s)	40.0
Horizontal viscosity coeff.	30.0

Table 6.7 : Computational parameters used in the TRIM3D model for case C.

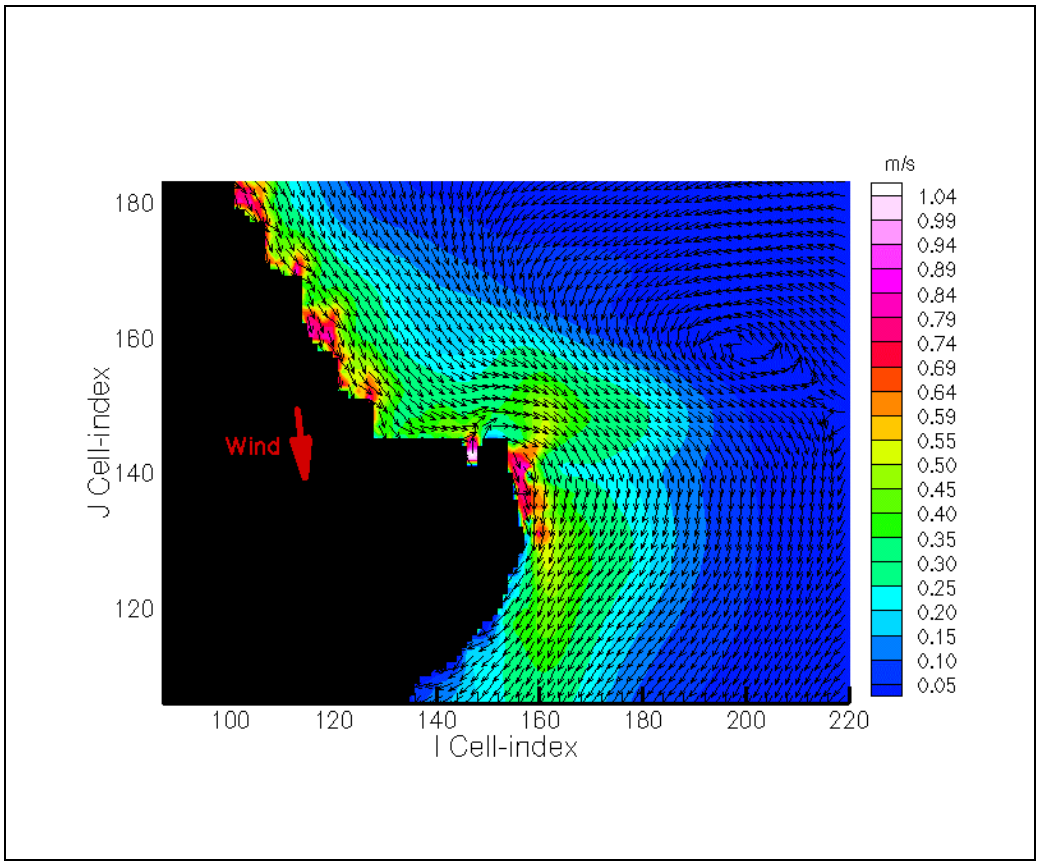

Figure 6.41: Circulation pattern at the Ebre delta area in the case defined by the parameters in table 6.7.

The transport parameters used in the dispersion model run are given in table 6.8 below. Several runs were made with varying constants for the horizontal dispersion coefficients, in the range 500-750, but the resulting particle distributions did not differ significantly; the coastal region occupied by the Lagrangian elements largely agrees with the plume's digitised contours in all cases. One of the concentration distributions obtained in the simulations (c_L = 500.9, c_T = 700.0) is shown in figure 6.42.

Parameter	Value
Total simulation time (hrs)	24.0
Computational timestep (sec)	5.0
c_L (Longitudinal dispersion constant)	500.9
c_T (Lateral dispersion constant)	700.0
c_V (Vertical dispersion constant)	0.16
Final number of particles	34600

Table 6.8: Parameters used in the LIMMIX model run corresponding to case C.

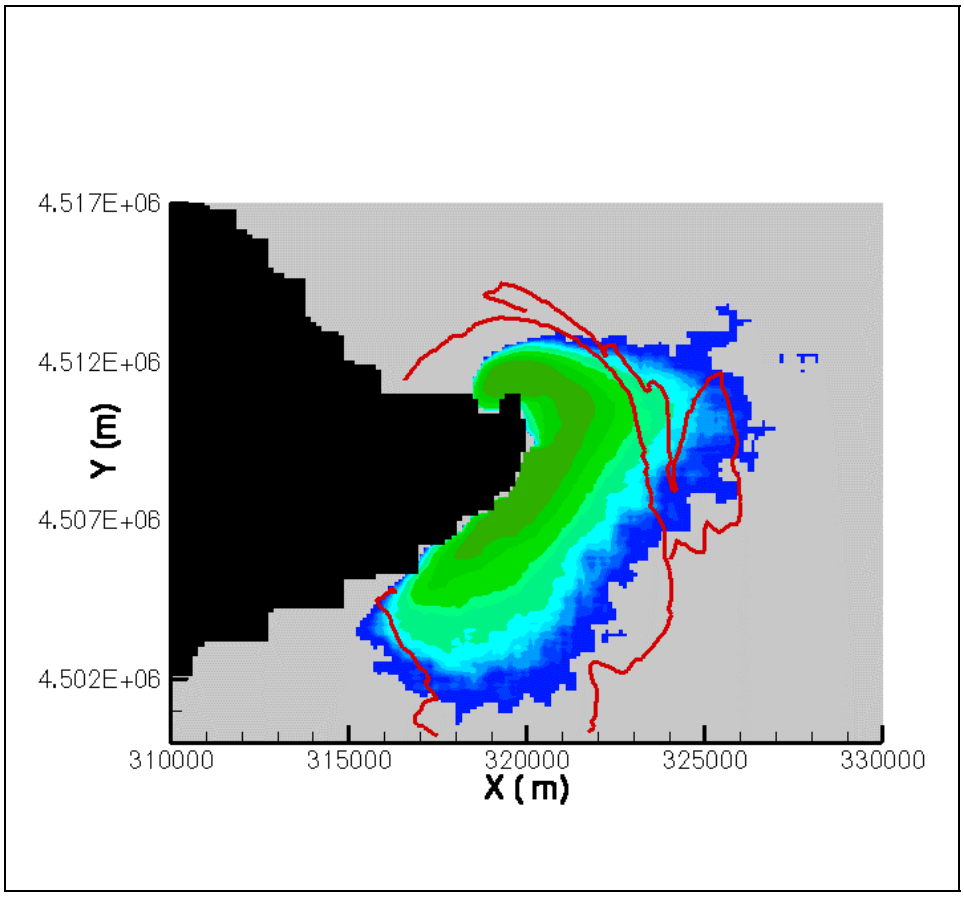

Figure 6.42: Plume resulting from the simulation of the Ebre river freshwater discharge, corresponding to case C. The solid lines correspond to the plume boundaries, digitised from the satellite image. Contours correspond to isohalines.

6.4 THE TARRAGONA HARBOUR (SPAIN)

The city of Tarragona is located at a latitude of 41º5' N and a longitude of 1º15' E, on the Spanish Mediterranean coast, between the delta of the river Ebre and Barcelona. The most important industries in the area are agriculture and petrochemical transformation and manufacturing, both of which are fully served by the city's harbour (Port de Tarragona). In 2000, the total traffic in the Port amounted to approximately 28,000,000 tons, of which over 17,000,000 tons corresponded to liquid bulks (92% petroleum and refined products), and over 9,000,000 tons were solid bulks (37.5% agricultural products).

The area occupied by the harbour is about 1,000 Ha.; the water depth inside the harbour ranges from 10 to 25 m. The river Francolí discharges inside the harbour area (figure 6.43), generating some concern about the fate of the transported sediment load, because of the slow rate of water renovation within the harbour. An attempt has been made to simulate the current fields in the harbour, and to use them to assess the transport of the river-borne sediment, under different meteorological, hydric and numerical conditions.

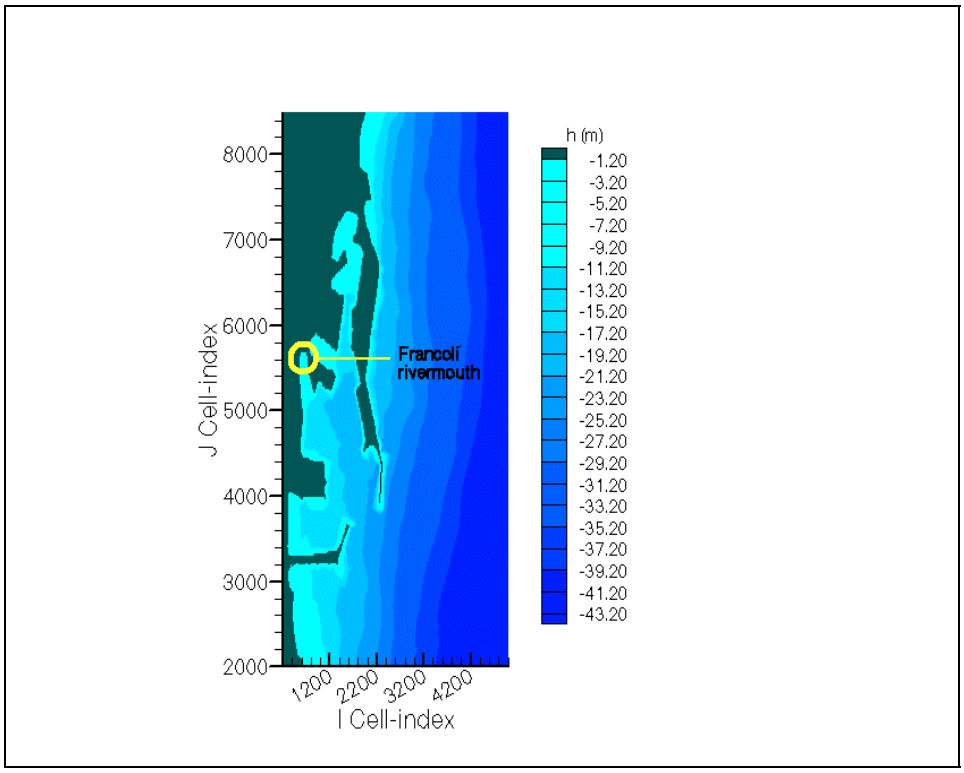

Figure 6.43: The Tarragona harbour, with the Francolí river mouth.

6.4.1 Modelled cases

The size of the chosen computational domain was 3,282m in the across-shore (x-)direction, and 8,970m in the alongshore (y-)direction; a 220x300-node grid was superimposed on the area, giving computational cells with Δx = 14.98m and Δy = 30m, and allowing a good resolution within the harbour. The underlying mesoscale circulation was not considered, and only the wind- and river-induced circulation was taken into account.

Four different cases were defined according to the magnitude of the freshwater discharge into the harbour and the direction of the incident wind and the. Two different river regimes were assumed, one corresponding to a maximum freshwater discharge rate of 1750 m^3/s (estimated for October 10^{th}, 1994), and one corresponding to the mean maximum flow measured between 1974 and 1990, Q = 32.4 m^3/s. Two different wind fields were used, defined by the direction and the speed of the wind. For the first wind field, a wind blowing from the NW, with u_w = 21.6 m/s, was chosen; the direction corresponds to the predominant wind in the area, and the velocity is close to the annual maximum. The second wind field was defined by a weaker wind (u_w = 10.3 m/s), blowing from the S.

The hydrodynamic field inside the harbour was obtained using the TRIM numerical model, which has been described before in this chapter. The computational domain has been divided into two layers, of which the upper one occupies the first meter closest to the surface (figure 6.44), and the lower one (figure 6.45) the rest of the waterdepth.

The transport of the suspended sediment dragged into the harbour waters by the river freshwater is modelled using the LIMMIX numerical code. The sediment grain has been assumed to have a mean diameter of 0.03 mm and a mean density of 2.54 g/cm^3. The suspended sediment concentration in the river freshwater entering the harbour is taken to be 26.7 mg/l; these parameters are based on studies by CEDEX (1993).

In addition, different values for the reflectivity indices were given to the computational cells nearest to the river mouth, for the cases with a larger freshwater discharge, in order to account for the resuspension due to the large bottom shear stress. A fully absorbent (a_{ij} = 0), a partially reflective (a_{ij} = 10) and a variably reflective scenario were tested, although only the former and the latter are presented here.

The simulation period in all cases is 12 hours, using a 0.5 sec timestep; the dispersion coefficients used are those proposed by Elder (1959) and Holly (1985) $-cu_*h-$ with the constants c equal to 5.91, 0.23 and 0.16 for the longitudinal, lateral and vertical dispersion, respectively. Because the upper hydrodynamical layer is thin compared to the total waterdepth, and the sediment deposition is governed mainly by the bottom currents pattern, only the lower hydrodynamical layer has been used in the transport simulation. The seawater density has been set as 1.02479 g/cm^3.

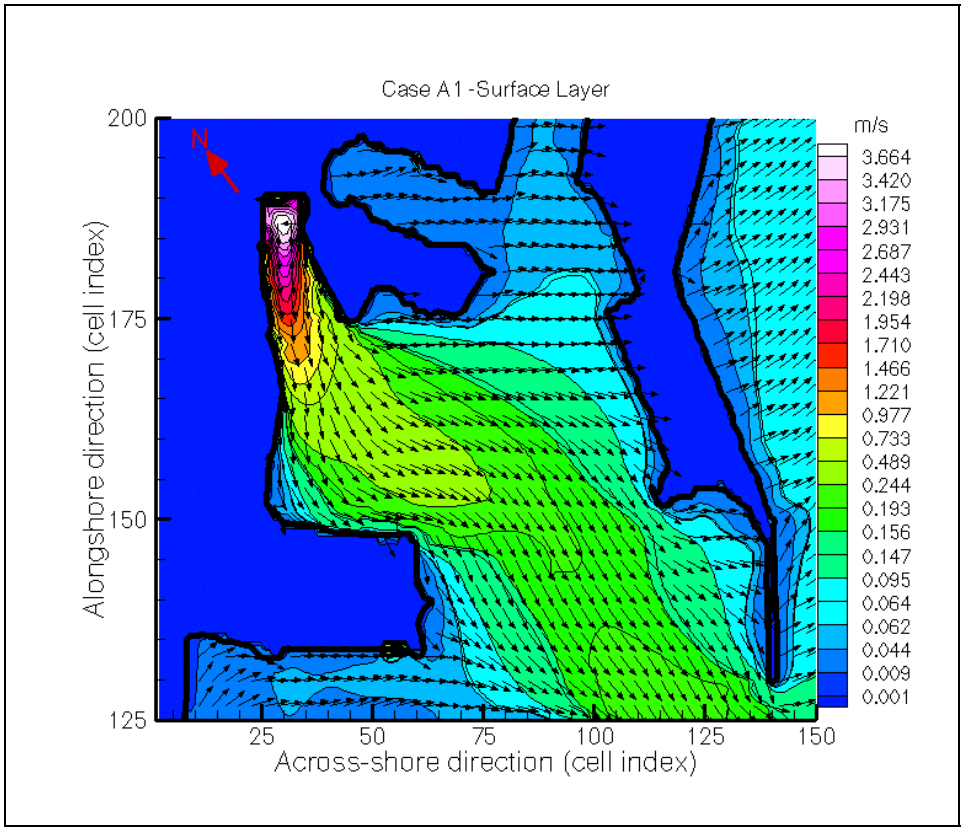

Figure 6.44: Hydrodynamic field in the Port de Tarragona, for Case A1. Surface layer.

6.4.1.1 Case A1 (Q=1750 m^3/s, u_w=21.6 m/s)

It is clearly seen that the current field inside the harbour is strongly dominated at both levels by the river discharge, whereas it is mainly wind-driven in the outer region. Away from the river influence, the effects of the wind on the upper layer (h =1m) inside the harbour are also evident, while the circulation pattern in the bottom layer (figure 6.45) is slightly more complex due to its interaction with the bathymetry.

Outside the harbour, the circulation in the upper layer (figure 6.44) is governed only by the wind stress, whereas the bottom currents are also influenced by the bathymetric characteristics.

The velocities inside the harbour are extremely large near the river mouth due to the large inflow of freshwater (corresponding to extreme discharge conditions); away from the river influence, the currents are much weaker, ranging from about 0.001 m/s in the bottom layer to about 0.06 m/s in the upper layer. Outside the harbour the modelled velocities range between 0.04 m/s and 0.14 m/s in the surface layer, and between 0.01 m/s and 0.03 m/s in the bottom layer.

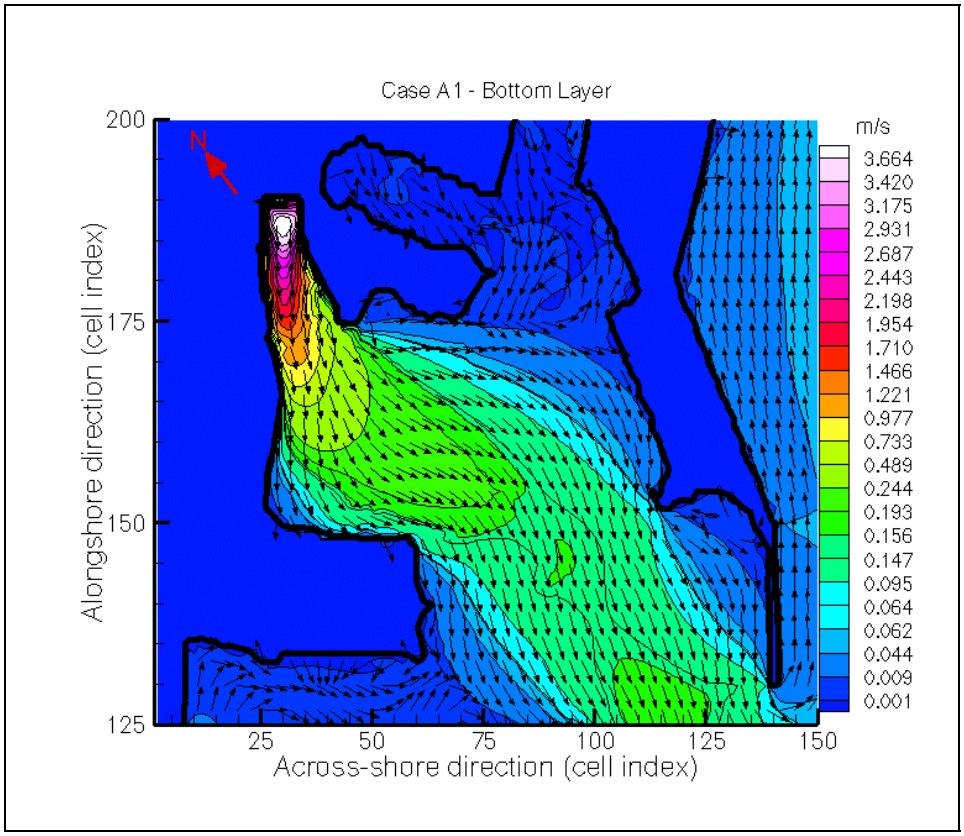

Figure 6.45: Hydrodynamic field in the Port de Tarragona, for Case A1. Bottom layer.

The results of the transport simulation model are shown in the figures below.The first figure (figure 6.46) corresponds to a totally absorbent sea bed, i.e., a_{ij} = 0. As expected, the sediment accumulates near the river mouth, since it becomes immobilised immediately after settling on the bottom.

Taking advantage of the strong river inflow, a simple and straightforward manner of simulating sediment resuspension has been attempted. Since the magnitude of the bottom shear stress induced by the freshwater discharge decreases with the distance to the river mouth, as the river water mixes with the receiving sea water, the resuspension process –and, therefore, the inability of sediment particles to remain on the sea bed- will be more intense near the mouth than further downstream. One way of reproducing this fact is to assign different values for the reflectivity coefficient a_{ij} at each cell, so that computational cells in the vicinity of the river mouth become less absorbent than cells farther away.

This procedure has been followed in the Tarragona harbour case, in order to assess its usefulness; the cells corresponding to the river mouth have been considered totally reflective (a_{ij} = 100), and the reflectivity coefficient has been taken to decrease linearly to a_{ij} = 0 (completely absorbent) five cells downstream from this point.

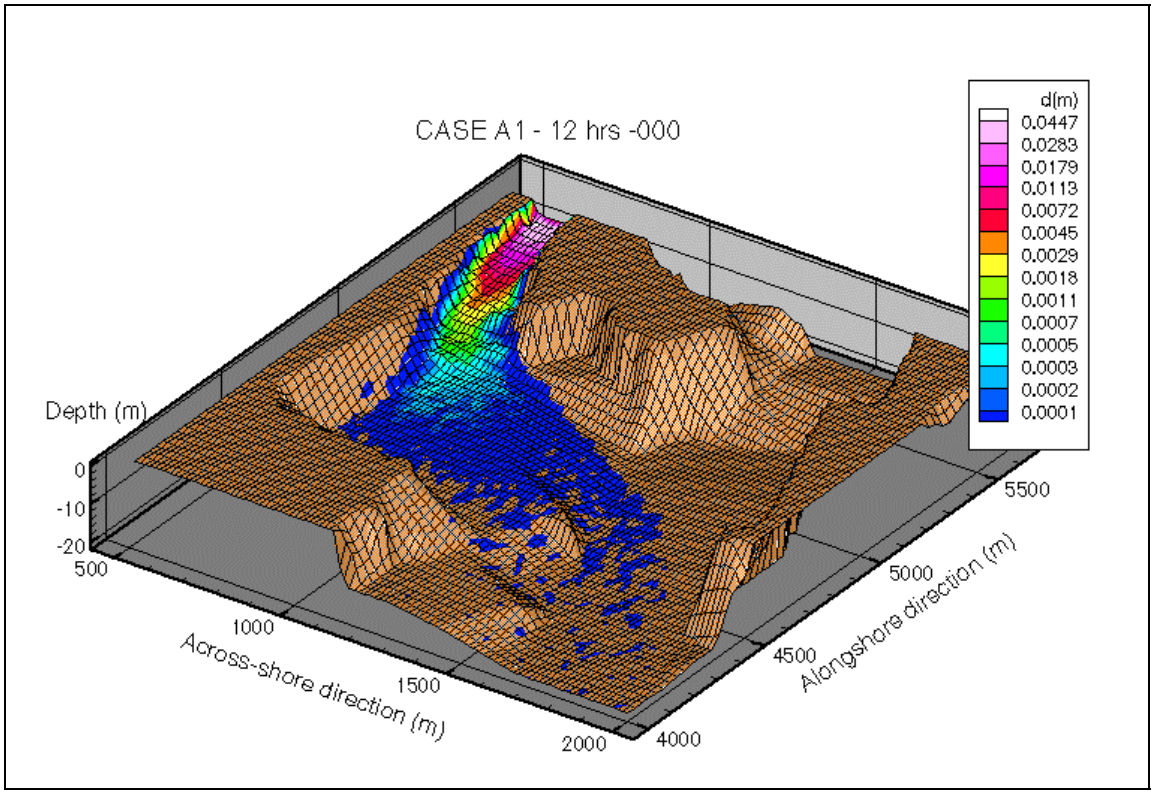

Figure 6.46: Sediment deposition for Case A1, after 12 hours, for a totally absorbent sea bed.

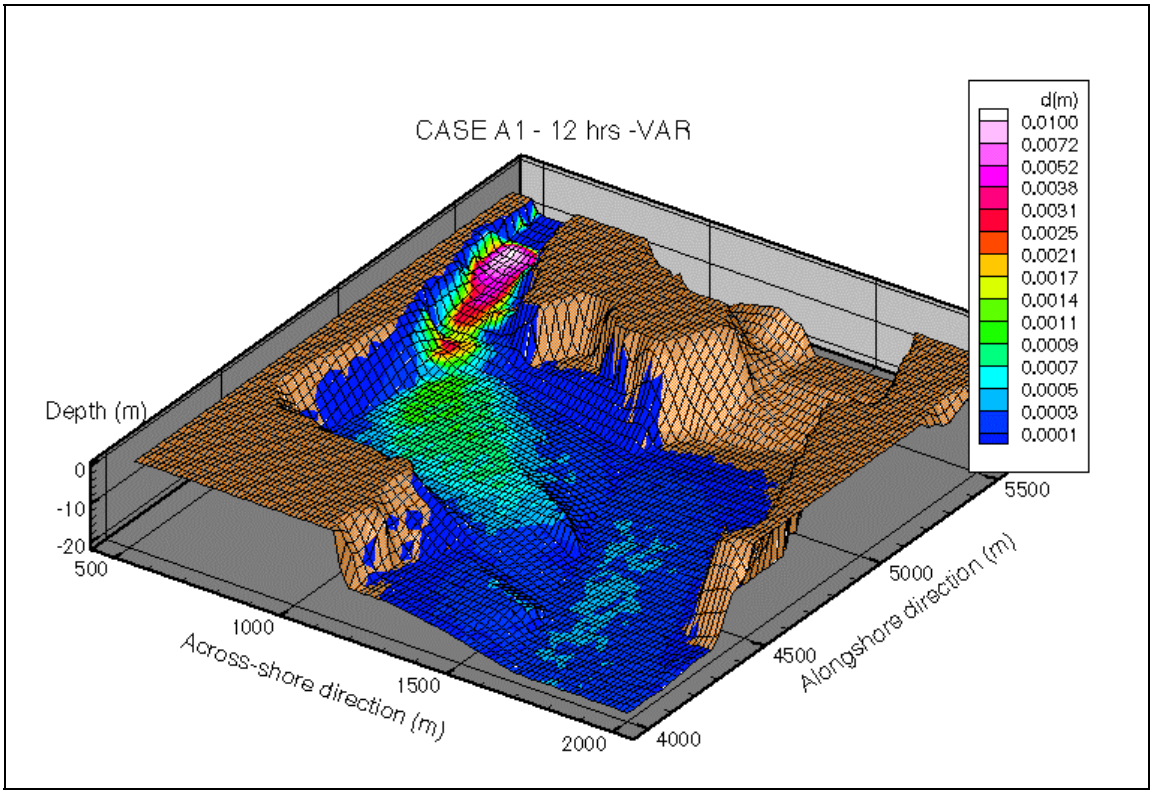

Figure 6.47: Sediment deposition for Case A1, after 12 hours, for a variably absorbent sea bed.

The differences between the sediment distribution at the end of the simulation for the case of a uniformly absorbent sea bed, and the case of a variably absorbent sea bed are clear in figures 6.46 and 6.47. In the latter case, maximum particle settling occurs not at the river mouth, but further downstream, and sediment particles are dragged farther away from the source -since they remain longer in the watercolumn-, leading to a thinner layer of sediment accumulating on the bottom

Although the results returned by the model seem to agree with the expected behaviour of the discharged sediment, the resuspension scheme adopted here should be further refined and tested to determine its validity –and range of application- as a simple and fast alternative to more sophisticated formulations which may burden the simulation (both time- and memory-wise). For instance, it is likely that the (linearly) variable reflectivity coefficient adopted here should in fact be a function of ratio between the ambient current and the sediment settling velocity, and such a dependence should be established in the future

6.4.1.2 Case B1 (Q=1750 m^3/s, u_w=10.3 m/s)

Again the computational domain has been divided in two layers, and the great influence of the river in both is the predominant feature inside the harbour. Compared to case A1, however, the river effects in the upper layer (figure 6.48) appear to be more restricted, due to the direction of the blowing wind, that acts against the freshwater flow. Nevertheless, the magnitude of the induced currents is again very large, as a consequence of the large flow of river water. The currents pattern in the bottom layer (figure 6.49) is very similar to that in case A1, indicating that the influence of the wind on the bottom circulation is negligible under the present river discharge conditions. The magnitude of the currents is also very similar to case A1.

Outside the harbour, where the effects of the river are non-existent, the circulation is purely wind-induced, and follows the isobaths in the lower layer. The magnitude of the velocity is smaller than in Case A1 due to the weaker wind used in this simulation.

The sediment deposition pattern in case B1 is very similar to that in case A1, due again to the predominant effects of the river outflow on the inharbour hydrodynamics. Figure 6.50 shows the sediment deposition for the fully absorbent sea bed. Comparing this figure with figure 6.46 it can be seen that the differences are minimum.

The same occurs when a variable reflectivity index is considered (figure 6.51), and the distribution of sediment in the harbour for case B1 appears also to be very similar to that found in case A1. Again, this is the result of the large river outflow, the effects of which considerably exceed the effects of the wind, virtually reducing two different cases to only one. As in A1, the mass of sediment transported into the harbour by the river is scattered over a much larger area when the reflectivity coefficient is assumed to vary with the distance to the river mouth, and so the thickness of the deposited layer is smaller than for a_{ij} = 0.

6.4.1.3 Case A2 (Q=32.4 m^3/s, u_w=21.6 m/s)

The hydrodynamic field obtained in this case reveals a much weaker influence of the river discharge on the currents inside the harbour, compared to the previous situation. It can be seen (figure 6.52) that the circulation pattern in the upper layer appears to be more complicated than in the case A1 because both the freshwater outflow and the wind play a role in driving the currents. The direct influence of the river is limited to the region closest to the mouth, with a maximum velocity of about 1.5 m/s in the surface layer. Outside the harbour, the currents's direction is determined by the isobaths, and the speed ranges between 0.005 m/s and 0.05 m/s.

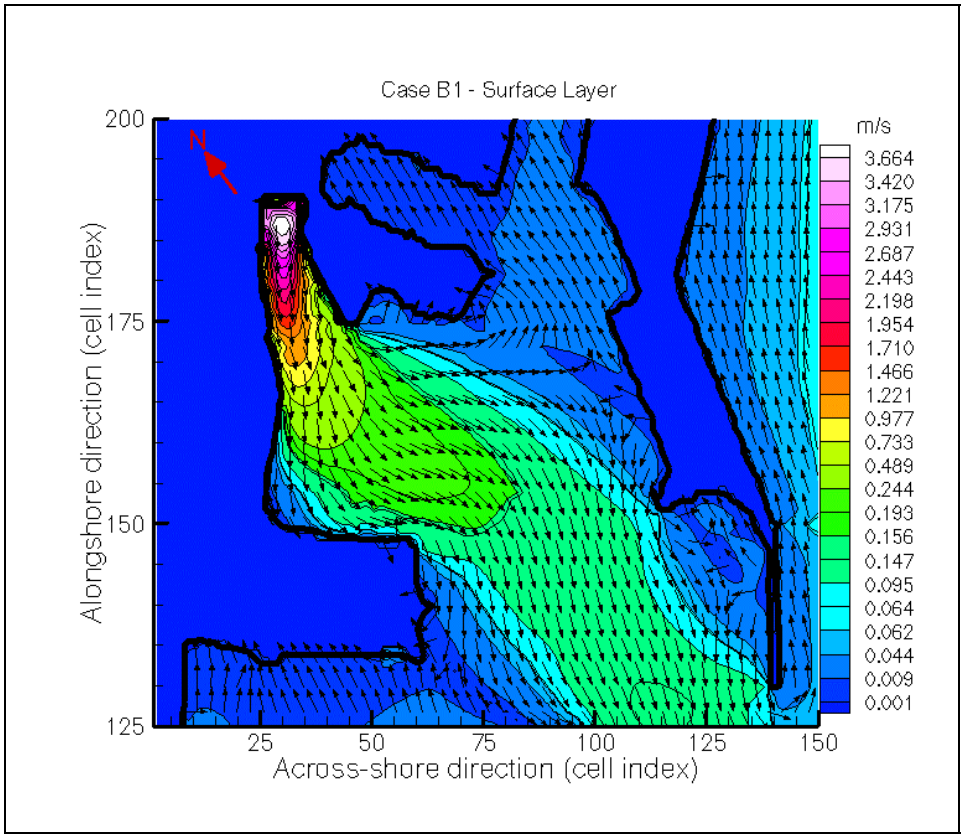

Figure 6.48: Hydrodynamic field in the Port de Tarragona, for Case B1. Surface layer.

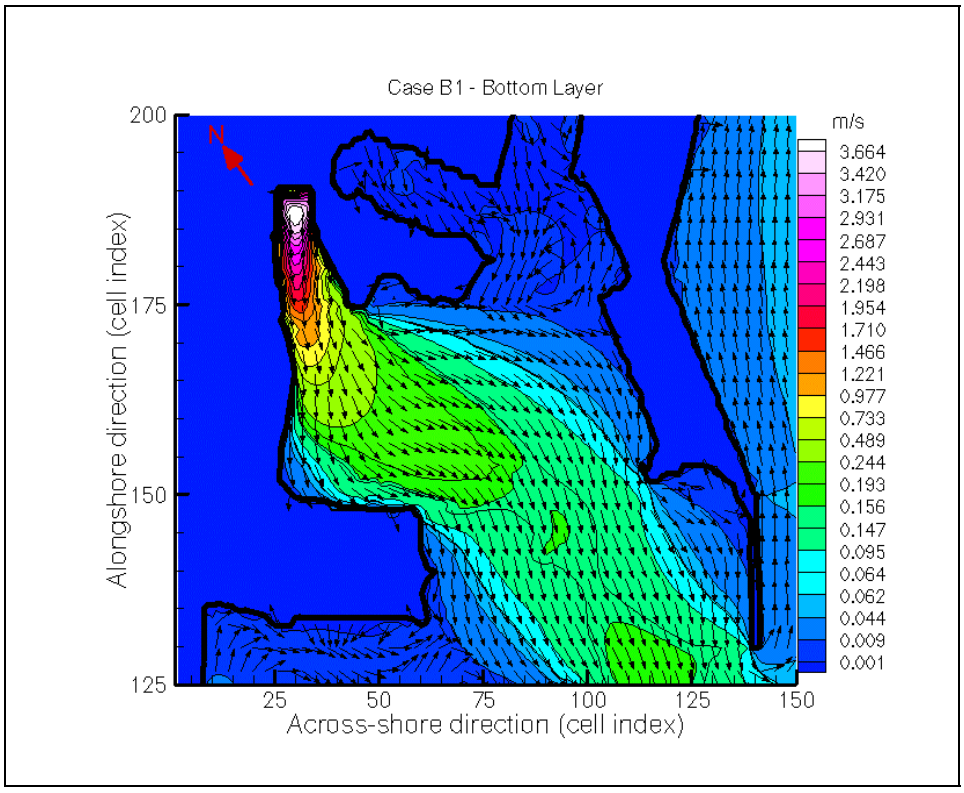

Figure 6.49: Hydrodynamic field in the Port de Tarragona, for Case B1. Bottom layer.

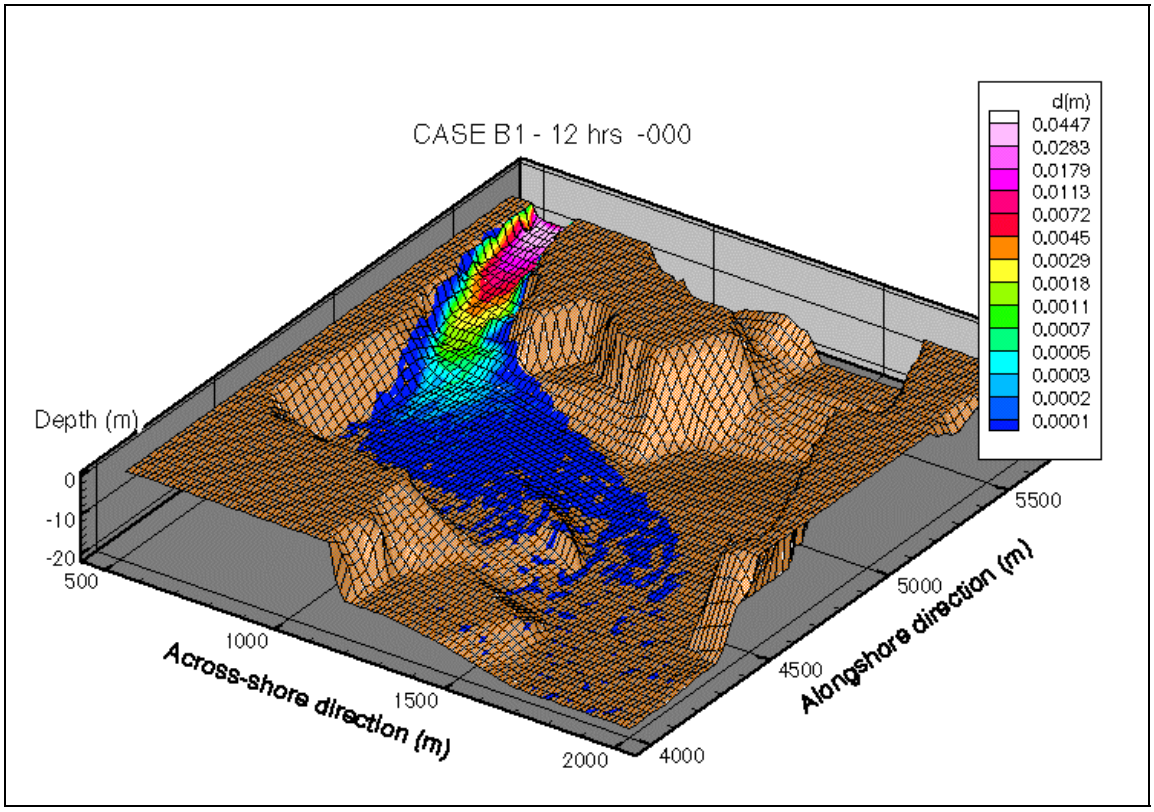

Figure 6.50: Sediment deposition for Case B1, after 12 hours, for a totally absorbent sea bed.

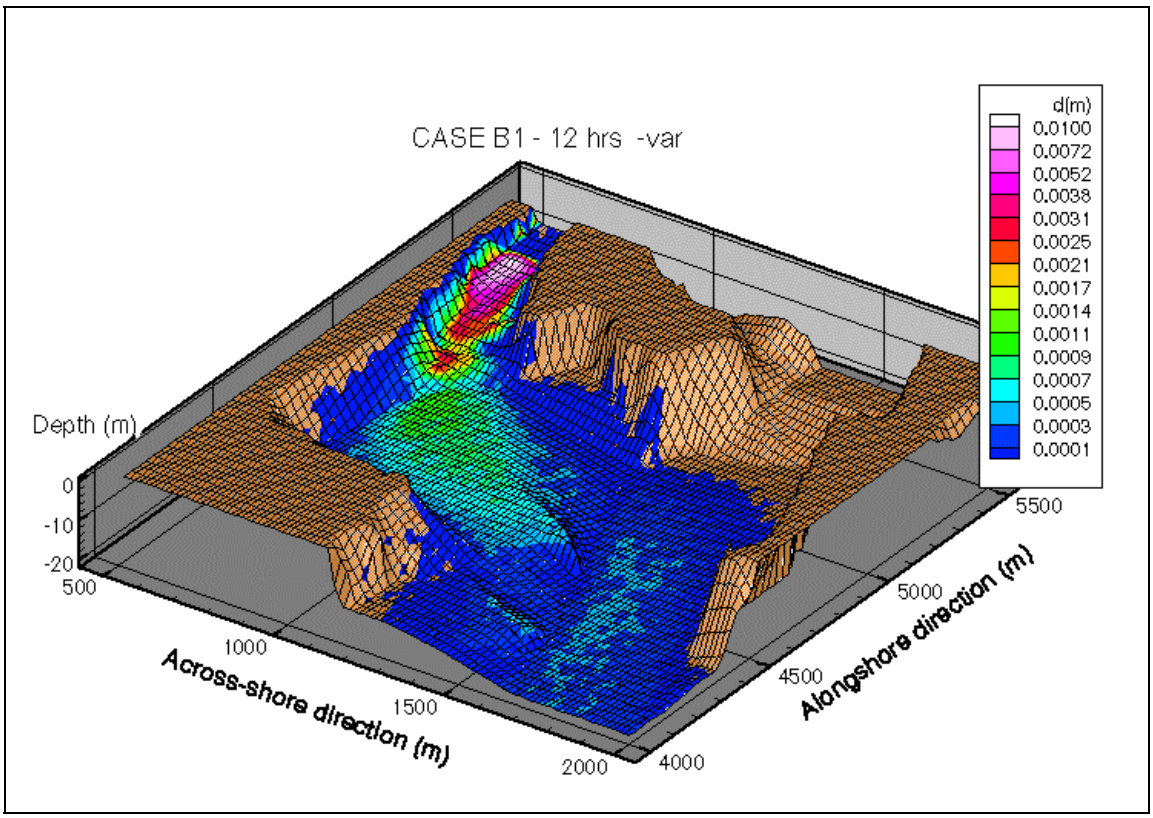

Figure 6.51: Sediment deposition for Case B1, after 12 hours, for a variably absorbent bed.

In the bottom layer (figure 6.53) the currents velocity inside the harbour lies between 0.2 m/s near the river mouth and about 0.001 m/s in the inner regions of the harbour, away from the river's influence. The influence of the freshwater discharge is again limited to the neighbourhood of the mouth, and the role played by the wind appears to be weak. However, a comparison between this case and the following one shows that the bottom circulation is strongly affected by the direction of the wind, since both current patterns clearly differ.

The general hydrodynamic field inside the harbour presents a clear dependence, as was expected, on the relative magnitude of the main driving agents. For river flows above 1,500 m^3/s, the effects of the wind on the waterbody are negligible, except in the areas sheltered from the river effects. The latter dominate the circulation over the whole waterdepth in most of the harbour, reaching up to the harbour mouth, and farther away. On the other hand, river discharge flow rates under 50 m^3/s reduce very much the effects of the freshwater momentum, allowing a larger influence of the wind on the currents both at the surface and bottom levels.

The simulation of the sediment transport for this case is shown below (figure 6.54), assuming a completely absorbent sea bottom. The distribution of river-borne sediment is limited to the area closest to the river mouth, because of a weaker discharge velocity than in the previous cases; additionally, the thickness of the sediment layer on the sea bed is also smaller than in cases A1 and B1, due to the smaller volume of discharged sediment particles.

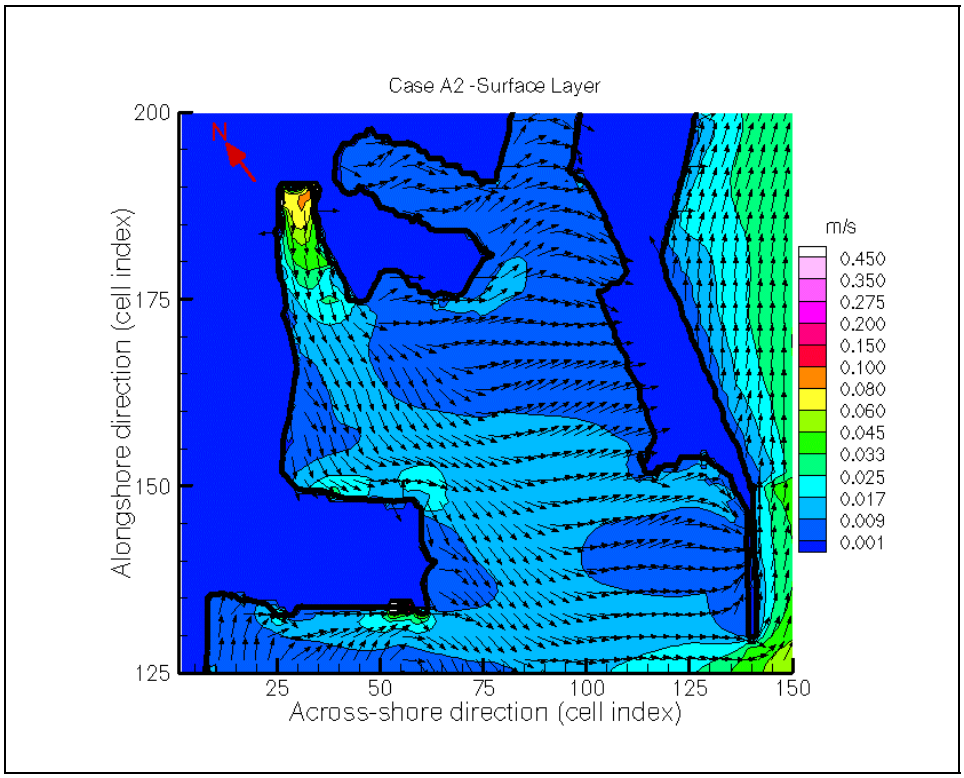

Figure 6.52: Hydrodynamic field in the Port de Tarragona, for Case A2. Surface layer.

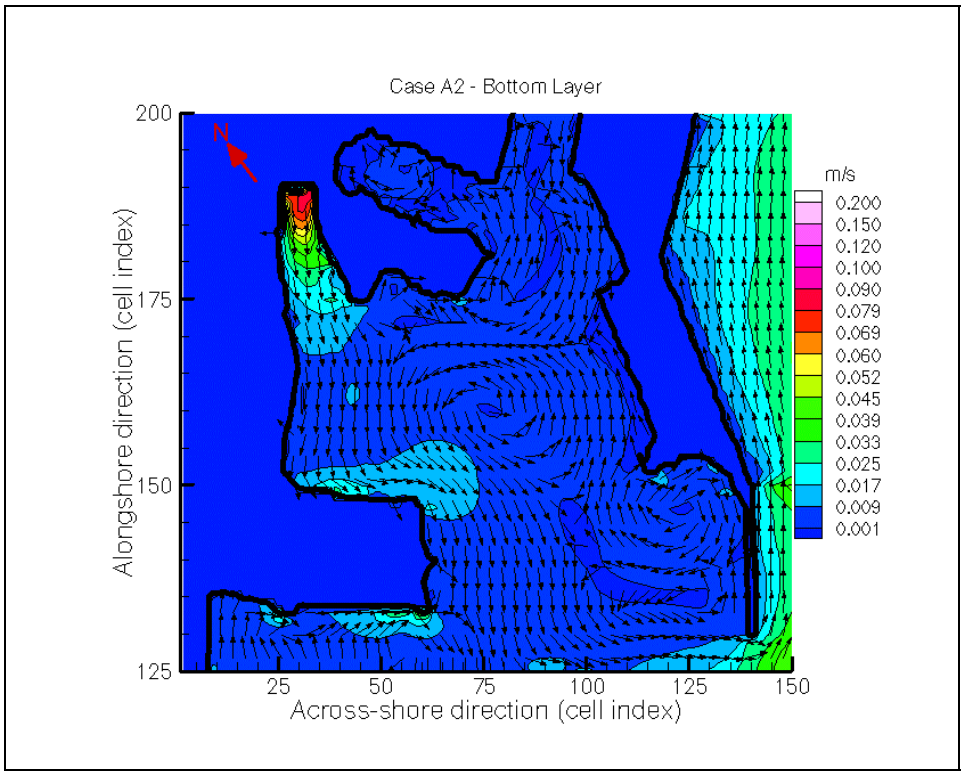

Figure 6.53: Hydrodynamic field in the Port de Tarragona, for Case A2. Bottom layer.

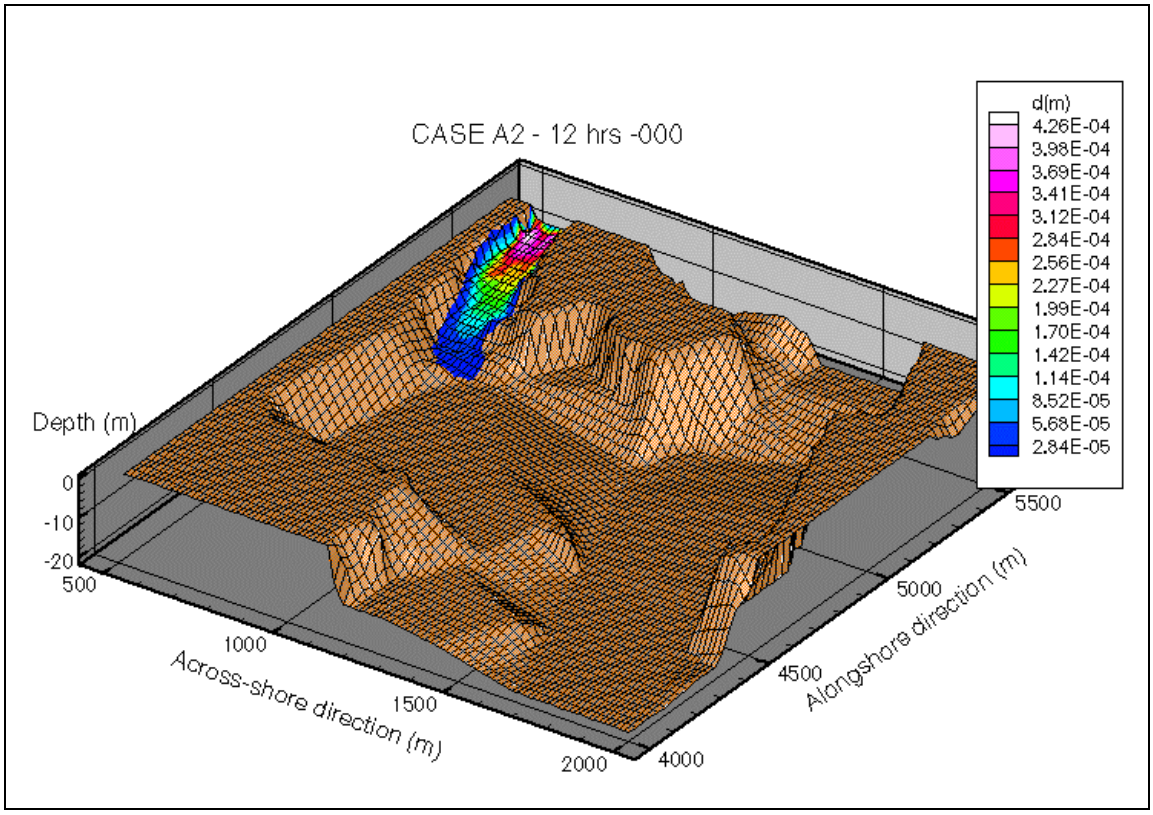

Figure 6.54: Sediment deposition for Case A2, after 12 hours, for a totally absorbent sea bed.

6.4.1.4 Case B2 (Q=32.4 m^3/s, u_w=10.3 m/s)

As in case A2, the influence of the river is much less important inside the harbour than in cases A1 and B1, obviously due to the smaller discharge flow. The relatively larger influence of the wind, blowing from the South, leads to a more complicated current pattern in the surface layer (figure 6.55) than the one obtained in case B1, including the presence of several small eddies, generated by the interaction between the wind-driven seawater entering the harbour and the circulation driven by the river discharge. The magnitude of the currents are much smaller than in case B1 (due to the smaller river outflow), and smaller than in case A2 (due to the weaker wind, and its direction), being very low away from the river mouth .

The bottom layer (figure 6.56) also presents clear differences with respect to the previous cases. The wind-induced currents enter the harbour on the sides of the port entrance, whereas the river-induced flow exits through the centre, generating eddies that might play an important role in trapping the sediment discharged by the river Francolí.

The transport model output for this case (figure 6.57) is very similar to that obtained for case A2. The settling of sediment particles is completed in the area nearest to the discharge point, although the sediment layer is again very thin compared to the cases for which the river discharge is 1750 m^3/s.

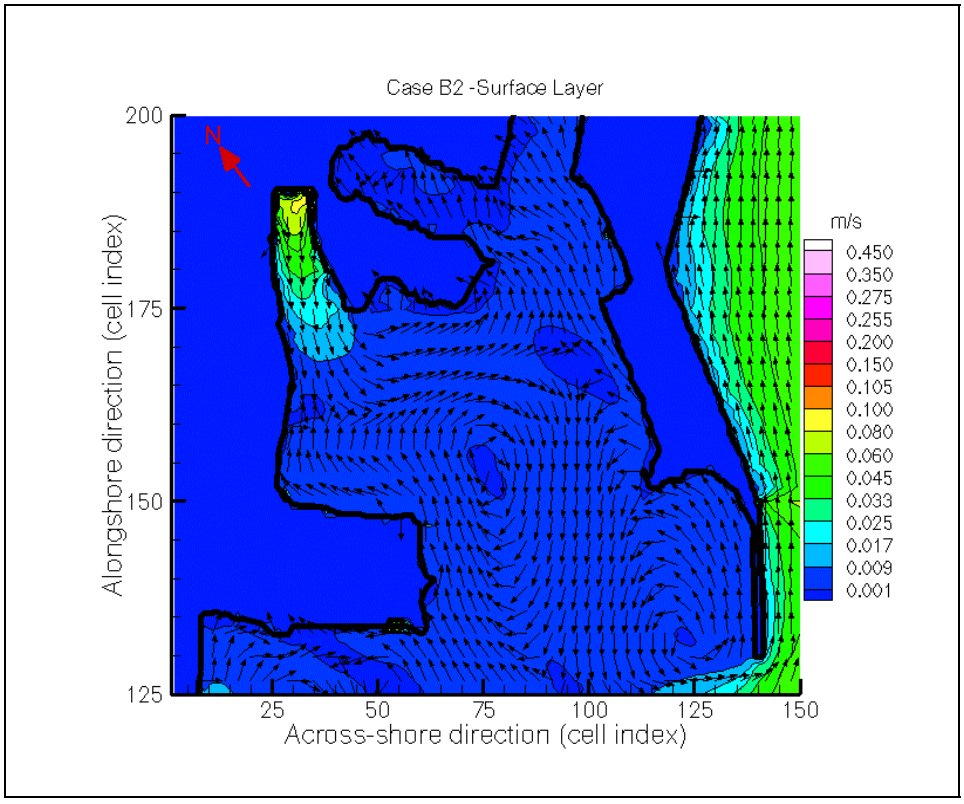

Figure 6.55: Hydrodynamic field in the Port de Tarragona, for Case B2. Surface layer.

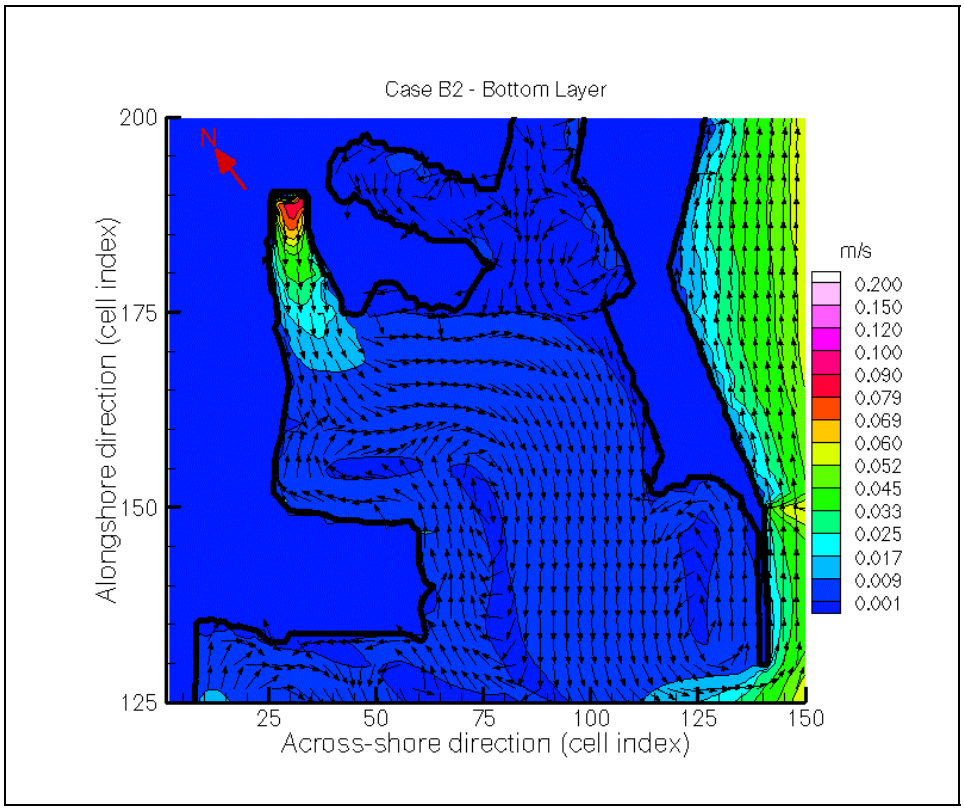

Figure 6.56: Hydrodynamic field in the Port de Tarragona, for Case B2. Bottom layer.

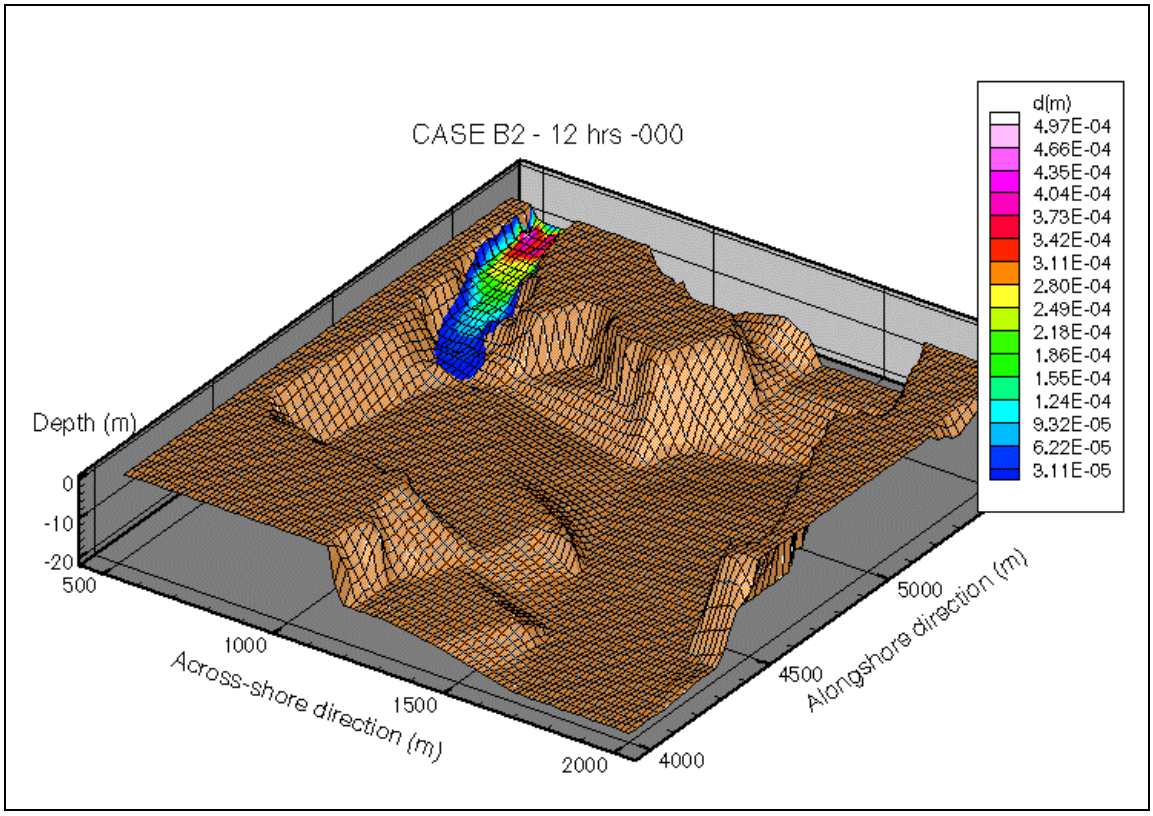

Figure 6.57: Sediment deposition for Case A2, after 12 hours, for a totally absorbent sea bed.

6.5 CONCLUSIONS

The numerical transport model LIMMIX has been applied to the simulation of four different real cases; of these, two allowed a direct comparison between modelled results and measured data, whereas the remaining two were limited to a qualitative evaluation of the results.

The first simulation is related to the wastewater discharge of a marine outfall off the coast of Barcelona (Spain). The outfall discharge is modelled under different ambient conditions, for one predominant wind field, and the behaviour of the resulting plume appears to be dependant on the waterbody density conditions. The qualitative analysis of the plume reveals that the simple buoyancy term used for the simulation was unable to reproduce in an accurate manner the buoyant forces acting on the wastewater, since it exhibits an excessively high rise velocity, and illustrates the need to develop a more efficient buoyancy module, such as the one presented in §5.2.1.3. On the other hand, and on a qualitative basis, the simulation of the initial discharge phase, and the merging of the individual plumes, appears to be acceptably reproduced by the model.

The second simulation case models the dispersion of a tracer patch in coastal waters, with the aid of digitised videotape frames. In this case, the evolution of the patch characteristics, such as its trajectory and diameters, are obtained from image digitalisation, and the obtained data is compared to the modelled results. It is observed that the coefficients which describe the dispersion of the patch are functions of time, and that their time dependency is different for the longitudinal and for the lateral coefficient, probably owing to the effects of the incident wave field, which in this particular case is parallel to the patch trajectory. The modelled path, and the time evolution of the tracer patch size, reproduce the observed patch characteristics to an acceptable degree.

The simulation of the river Ebre's freshwater plume is the goal of the third real case. Different wind fields and river discharge rates were considered and, as in the first case, the simulation combined the results provided by a hydrodynamic model and those from the transport model, to yield salinity distributions, which are then compared quantitatively to data measured *in situ*, and quantitatively to the plume observed in a satellite image. The match between the obtained results and the measured salinity values is acceptable in one case, with differences of the order of 10%, but appears to be not so satisfactory in the other case, for which the differences are larger, of up to 80%. However, the particular distribution of the salinity revealed by the field measurements in this latter case suggests that either the process of field data acquisition was subject to some type of error, or that an important contribution to the mixing of the riverine freshwater in the coastal region was due to some mechanism not included or considered in the model (e.g., non-stationary wind fields, etc.). Again, the sensibility on the integration variable of the mapping module used to transform the discrete particle distribution to a continuous concentration distribution is evident in this case. The third simulation attempts to compare the modelled plume with one observed on a SPOT image; here, the overall shape of the simulated plume generally reproduces the shape of the real plume, although the internal structure of the plumes has not been resolved. Elder's (1959) horizontal dispersion coefficients have been used for these river plume cases, and the simulations appear to be acceptable when the parameters c_L = 500-1,000 and $c_T \approx 700$ are used.

Finally, the fourth case simulates the fate of sediment discharged by the river Francolí into the Tarragona harbour. The results from the simulation cannot be compared to measured data, since no measurement are available inside the harbour, so a qualitative analysis has been done. The sediment transport has been modelled for two different wind conditions, and for two different river discharge rates. The results reveal that the influence of the wind on the sediment transport is almost negligible for both freshwater discharge rates. When the river outflow is large ($Q \cong 1{,}000$ m^3/s or more) the hydrodynamics within the harbour are driven mainly by the river momentum; on the other hand, for smaller freshwater flows ($Q \cong 100$ m^3/s), although the circulation pattern is driven predominantly by

the wind over the whole watercolumn, particle settling appears to occur very close to the river mouth, where the momentum of the freshwater discharge is still the dominant current-driving mechanism. The simulation has considered different values of the reflectivity coefficient in the vicinity of the river mouth in order to include sediment resuspension, and the differences between a totally absorbent and a variably absorbent bottom are quite considerable.

In summary, the modelling of these four real cases proves the versatility and capabilities of the model, allowing the simulation of a wide range of situations. On the other hand, the application of LIMMIX to both real and theoretical cases reveals, however, the dependence of the numerical results on both physical –conceptual- and numerical features, such as the closure submodels used, the hypotheses introduced to solve the equations, or the values of some user-definable variables. Nevertheless, improvements in both aspects are